Editors' Suggestion

Towards trapping of hydrogen atoms for computable optical clock applications

O. Amit[1,*] D. Taray[1] V. Wirthl[1] V. Weis[1] M. W. Syed[1] A. Ozawa,[1] J. Weitenberg[1,2] S. G. Karshenboim[1] J. T. M. Walraven[3] L. Maisenbacher[4] R. Pohl[5] Z. Burkley[6] F. Schmid[7] T. W. Hänsch,[1,8] D. C. Yost[9] and Th. Udem[1,8]

[1]*Max Planck Institute of Quantum Optics, Hans Kopfermann Strasse 1, 85748 Garching, Germany*
[2]*Fraunhofer Institut für Lasertechnik, Steinbachstrasse 15, 52074 Aachen, Germany*
[3]*Universiteit van Amsterdam, Van der Waals-Zeeman Instituut, Science Park 904, 1098 XH Amsterdam, The Netherlands*
[4]*Department of Physics, University of California, Berkeley, Berkeley, California 94720, USA*
[5]*Institut für Physik, QUANTUM, Johannes Gutenberg-Universität, Staudingerweg 7, 55128 Mainz, Germany*
[6]*Institute for Particle Physics and Astrophysics, ETH Zürich, 8093 Zürich, Switzerland*
[7]*Institute for Quantum Electronics, ETH Zürich, 8093 Zürich, Switzerland*
[8]*Fakultät für Physik, Ludwig-Maximilians-Universität, Schellingstrasse 4, 80799 München, Germany*
[9]*Department of Physics, Colorado State University, Fort Collins, Colorado 80523, USA*

(Received 11 April 2025; accepted 5 August 2025; published 2 September 2025)

Because of its simple structure, the hydrogen atom is often used as a testbed for quantum electrodynamics. Spectroscopy of trapped atomic samples can greatly improve the accuracy of these tests. Trapping atomic hydrogen in an optical dipole trap or an optical lattice has never been achieved. Only trapping in magnetic fields that lead to large Zeeman shifts has been demonstrated. Standard techniques of atomic physics are difficult to apply to atomic hydrogen. The small mass of the atom and the large photon energy of the 1*S*-2*P* cooling transition significantly complicate Doppler cooling. This proposal introduces a photon recoil-assisted loading scheme that uses these properties to our advantage to load atomic hydrogen into an optical dipole trap without laser cooling. The magic wavelength (515 nm) for the 1*S*-2*S* clock transition (1.3-Hz natural linewidth) is easily accessible with current laser technology. Since the 1*S*-2*S* clock transition can be driven Doppler free, we do not require a very low temperature. Besides improving spectroscopy for fundamental science, such a system can also be used as a "computable" atomic clock that may one day justify the redefinition of the SI second in terms of the Rydberg constant.

DOI: 10.1103/3bnr-q23f

I. MOTIVATION

The discrete line spectrum of atomic hydrogen has been the Rosetta Stone for the development of quantum mechanics. As the simplest of all atoms, hydrogen allows for the most precise calculations. Classical physics fails to describe the hydrogen atom. The discrepancy between classical physics and experimental observations gave rise to the first quantum model by N. Bohr [1]. In large parts, atomic hydrogen was key to developing quantum mechanics. Subsequent refinements led to the quantum theories of E. Schrödinger and P. A. M. Dirac. Another famous discrepancy between Dirac's theory and observations discovered by W. E. Lamb and R. C. Retherford [2] led to the most accurate theory in all of physics so far, the theory of quantum electrodynamics (QED).

QED is part of the Standard Model and serves as a blueprint for all quantum field theories therein. The precise determinations of transition frequencies of simple atomic systems are required to test QED. The sharpest transition in atomic hydrogen occurs between the 1*S* ground state and the metastable 2*S* state with a natural linewidth of only 1.3 Hz. Its transition frequency has been measured with almost 15-digit accuracy using an optical frequency comb and a cesium atomic clock as a reference [3]. However, the first laser measurement of the Lamb shift in muonic hydrogen was found in significant contradiction to the hydrogen data obtained until then [4,5]. Today, improvements in experimental techniques, such as the optical frequency comb [6], continue to add more digits to the measured transition frequencies [7–9] that can be compared with ever-improving theoretical calculations. Such a comparison acts as a probe for physics beyond the Standard Model [10–13].

Atomic hydrogen has an attractive level scheme for an optical clock. Since there is no 1*P* state, the 2*S* state can neither decay nor be excited with a single (optical) photon dipole transition, at least not in a field-free environment. This has three important advantages: The natural linewidth of $A/2\pi = 1.3$ Hz, combined with the high transition frequency of $\nu_{\text{clock}} = 2\,466$ THz, leads to a quality factor of

*Contact author: omer.amit@mpq.mpg.de

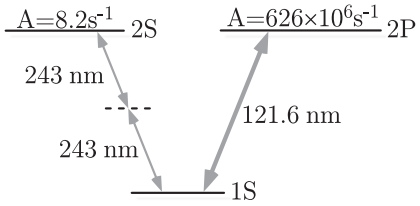

FIG. 1. Simplified level scheme (without fine- and hyperfine-structure) of atomic hydrogen with decay rates A and transition wavelengths. The two-photon transition from the 1S ground state to the metastable 2S state serves as the clock transition. The 2S and 2P levels have almost degenerate energies.

$Q = 2\pi\,\nu_{\mathrm{clock}}/A = 1.9\times10^{15}$, similarly to the quality factor of the Ca^+ clock [14]. Because the 1S-2S clock is excited with two photons as sketched in Fig. 1, the probe laser operates at 243 nm rather than 121.6 nm (Lyman-α). Last, the two-photon excitation can be arranged such that it is free of the first-order Doppler effect. This eliminates a set of systematic effects.

The main experimental limitation has been the difficulty of laser cooling atomic hydrogen because no simple continuous wave laser can address the 121.6-nm Lyman-α 1S-2P Doppler cooling transition (see Fig. 1). Additional challenges are the low mass, the rather large linewidth of the cooling transition ($A/2\pi = 100$ MHz), and the energetically allowed ionization from the 2P state by the cooling laser. The latter problem persists even when cooling with a two-photon transition. Using the 1S-2S transition for two-photon cooling does have the additional problem of an extremely low scattering rate. Several proposals to solve these issues have been made [15–18]. However, none of these have been implemented yet for atomic hydrogen to the best of our knowledge.

We propose a new method to overcome this barrier and to load atomic hydrogen into an optical dipole trap (or optical lattice) without laser cooling using off-the-shelf lasers. Once in the trap, other cooling methods, like evaporative or adiabatic expansion cooling [19], may be applied. It turns out that for the exotic parameters of atomic hydrogen, the better strategy is to trap before cooling, while most other species need to be cooled before they can be trapped. An advantage of the 1S-2S clock transition is that it can be driven with two photons in a Doppler-free arrangement. In this case, the lowest temperatures are not required, but trapping is important for a long interaction time.

Our approach is based on magnetic deceleration within a cryogenic nozzle, velocity selective deflection, and a single recoil event from deexcitation within an optical dipole trap. Given the low mass, a single photon recoil can almost stop the atoms within the trap. Such a trap may operate at one of the magic wavelengths that cause identical light shifts to the ground and the excited states, providing a trapping potential without affecting the clock transition frequency [20,21]. The longest magic wavelength for the 1S-2S clock transition is at 514.646 nm [22]. Powerful and narrow-band lasers are readily available at this wavelength.

It should be mentioned that atomic hydrogen has been trapped in the past using superconducting magnetic traps [23]. These traps were also loaded without laser cooling. While a continuous wave Lyman-α laser is still very difficult with only microwatts of power available [24], simpler pulsed systems can have similar average powers albeit with ∼10 Hz repetition rates [25,26]. One cannot laser-cool atomic hydrogen from a thermal gas or an atomic beam with these parameters. However, laser cooling to 8 mK has been achieved when the atoms are already within a magnetic trap and exposed to the laser for 15 min [27]. The 1S-2S clock transition has been observed under these conditions [28], and even Bose-Einstein condensation was achieved [29]. This work is now being revived in other labs [30,31]. Other schemes of magnetic trapping use a Zeeman decelerator [32].

At CERN, the Antiproton Decelerator routinely allows the production and investigation of antihydrogen. Among others, the ground-state hyperfine splitting [33], the 1S-2S clock transition [34], and the gravitational acceleration have been measured [35]. Laser cooling of antihydrogen requires several hours of laser exposure [36]. This reemphasizes that cooling can only be achieved once the atoms are trapped. Reloading into an optical dipole trap and transporting antihydrogen out of the strong magnetic fields may be an option for future experiments. While antihydrogen is produced within the trap, we will have to load hydrogen first but expect a much higher initial density.

Superconducting magnetic traps are large and cumbersome setups that we do not consider suitable for clock applications that should be simpler and have the potential to operate with a large duty cycle without human intervention. In addition, the Zeeman shifts can pose a challenge to the expected accuracy. The current proposal aims to describe a path to load atomic hydrogen in an optical dipole trap that avoids this complication as well as the difficult Lyman-α laser. Besides this scheme, many researchers are working to solve this problem. Laser-cooled and dissociated diatomic hydrides [37–39] are an option. Similar ideas have been proposed for antihydrogen [40] by sympathetically cooling $\bar{H}^+$ ions [41]. Sympathetic cooling in a lithium MOT is another idea that has been proposed [42] as well as helium buffer gas and lithium-assisted evaporative cooling [43]. Buffer gas has also been suggested to be used with deep optical potentials to assist loading [44].

Redefinition of the second

One can achieve greater spectroscopic precision and potentially develop a hydrogen optical atomic clock by utilizing trapped atomic hydrogen. Based on the most basic stable atoms, this clock has been referred to as the first "computable clock" [45]. Its transition frequency can be linked directly to fundamental constants such as the Rydberg constant R_∞. Defining the value of the Rydberg constant would make it possible to establish a new SI second [46]. A similar proposal of a hydrogen optical lattice clock has recently been published by J. P. Scott [47] and coworkers, albeit without a method of loading the dipole trap, which is the focus of this work.

Fixing the values of constants with units is the best method to define these units because it separates the definition from the realization. For example, the new kilogram (kg) is based on the definition of the value of Planck's constant, the speed of light, and the Cs ground-state hyperfine splitting ν_{Cs}. Cur-

rently, two very different methods exist to realize the kg (using a silicon sphere or a Kibble balance). In the future, there can be other methods of realizing the kg that adapt to possible technological advancements without ever changing the definition. Another advantage is that different realizations can operate on vastly different scales, similarly to the realizations of the meter by laser interferometry on a micrometer scale and lunar ranging on a 10^8-m scale.

With the 2018 reform of the SI system, all but one of the units are now based on defined constants. The only remaining (natural) object is the cesium atom used to define and realize the SI second by fixing the value of ν_{Cs}. A natural way to proceed is to remove the last object from the SI by defining the value of the Rydberg constant. This fixes all atomic and molecular transition frequencies that can be expressed as a dimensionless theory expression multiplied by R_∞. The theory must be developed to compute these transition frequencies to use this possibility. Therefore, hydrogen is the first but not the only choice for the realization. Hydrogen-like helium ions can be held in an ion trap and sympathetically cooled using beryllium ions [48] and might also serve this purpose in the future [46].

Currently, the theory can predict hydrogen levels with an uncertainty of 10^{-13}, which excludes experimental uncertainties from constants. This precision is limited by higher-order nuclear effects such as polarizability and higher-order bound-state QED contributions. An unresolved issue is the lack of a precise value for the nuclear charge radii entering the theory (see, for example, Ref. [9]). Possible solutions are advancements in lattice QCD techniques that, in principle, allow the calculation of the charge radii [49]. Pure leptonic systems such as positronium and muonium could also solve this problem, but their short lifetime would limit the achievable accuracy [50,51].

A hydrogen clock may not be the most accurate compared to clocks based on other atoms (Sr, Yb) or ions (Al^+, Yb^+), as other optical clocks currently provide better stability and accuracy. However, with precise ratio measurements [52] involving the hydrogen clock, it is still possible to define the second using the Rydberg constant. That said, given that the gravitational redshift within the trapped atomic cloud is now the limiting factor [53], it may be that accuracy is no longer the sole criterion for evaluating a good clock.

II. SYSTEM OVERVIEW

In this section, we present an overview of the proposed setup before we discuss the details in the following sections. As sketched in Fig. 2, an atomic hydrogen beam is obtained from a cryogenic nozzle [54], described in more details in Sec. III. In contrast to our existing $1S$-$2S$ spectrometer [3], a collinear laser beam does not need to go through the nozzle. This gives us more freedom in the design to obtain a significantly larger atomic hydrogen flux. With our previous "T-shaped" nozzle (see for example [3,55,56]), atoms on-axis can only emerge from atom-atom collisions. As detailed in the next section, collisions are rare and so is the overall flux [56,57]. The atomic beam obtained with the nozzle sketched in Fig. 2, emerges from a 5 K cold surface of a permanent magnet after thermalizing on the surface. Hydrogen atoms are guided to the nozzle from a gas discharge that breaks up the molecules. Teflon tubing prevents the atoms from recombining into molecules.

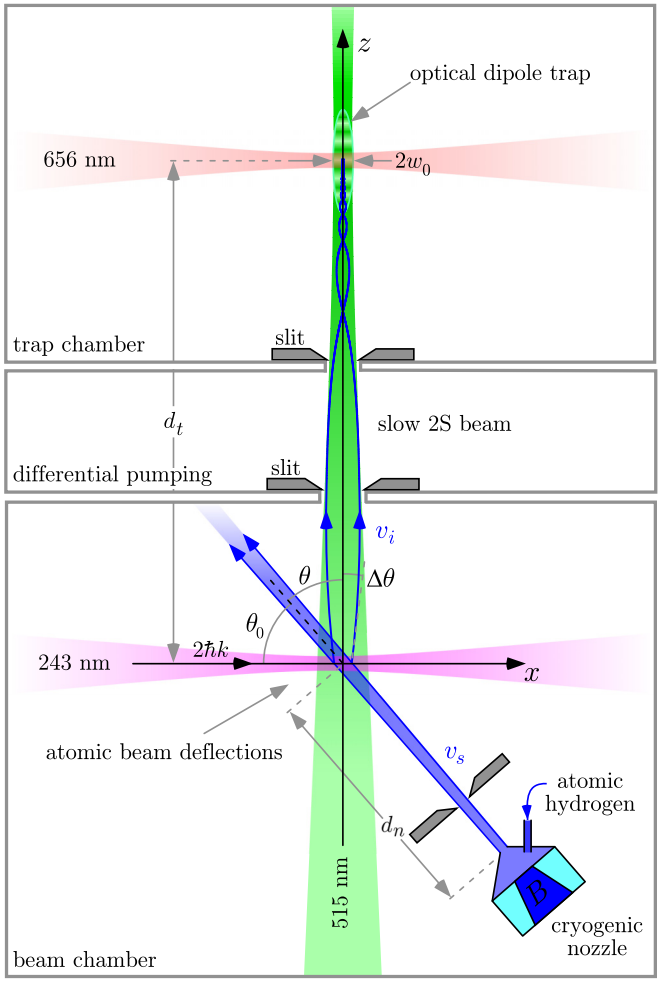

FIG. 2. A possible layout of the proposed hydrogen trap (not to scale). From the bottom to the top: A 5 K beam of atomic hydrogen is formed within the nozzle. The atoms emerge from the surface of a magnet, where the high-field-seeking atoms need to crawl uphill to escape. A 243-nm laser beam deflects some atoms by exciting them to the metastable $2S$ state. The deflection angle θ is velocity dependent. The angle is chosen such that atoms with an initial velocity v_s travel along the axis of the trapping laser (optical dipole trap at 515 nm) through a differential pumping section into an ultrahigh vacuum trap chamber. The trapping laser also acts as a waveguide for the $2S$ atoms. Two selected trajectories are plotted to show the oscillatory behavior of the atoms within the waveguide. The trapping laser perturbs the $2S$ atoms and causes some to return to the $1S$ ground state, predominantly at the trap center, upon which they receive a large photon recoil in a random direction. Some of these recoils have the proper direction so that the emitting atoms remain in the trap. The $1S$ ground state then no longer scatters trap-laser photons. An optional weak laser tuned close to the Balmer-α $2S$-$3P$ transition at 656 nm may be used for additional quenching and as a potential barrier. For the modeling, we assume the parameters: $v_s = 5$ m/s, $w_0 = 50\,\mu$m, $d_n = 10$ cm, $d_t = 30$ cm as well as 6 W and 1 kW of laser power at 243 and 515 nm, respectively. The nozzle radius is assumed to be $R_n = 0.5$ mm. The final design may use different parameters as we optimize the system.

Upon leaving the nozzle, the high-field-seeking atoms are slowed down so that their number in the slow tail of the Maxwell-Boltzmann distribution is enhanced (see Sec. III B). Some slow atoms are later removed by collisions with the faster atoms within the beam. This is known as the "Zacharias effect" [58,59], as discussed in Sec. III A.

The atomic beam then crosses a laser beam at 243 nm, enhanced in a resonator, that drives the $1S$-$2S$ two-photon transition. The laser light is tuned to the Doppler-sensitive component, where two photons from either direction are absorbed. This gives the atoms a recoil along the x axis. The velocities are thereby dispersed as discussed in Sec. IV. The undeflected and reverse-deflected atoms (not shown in Fig. 2 for clarity) can be employed for normalization. Such a normalization was previously essential for high-quality data in our $1S$-$3S$ experiment [8]. A range of velocities can be selected using a series of slits, skimmers, or a long and narrow tube acting as the separator for differential pumping between the beam chamber with high-vacuum and the ultra-high-vacuum (UHV) trap chamber. Very low pressures ($<10^{-8}$ mbar) are required for stable trapping. Additional differential pumping around the nozzle and a gas catcher might be required.

We do not know the lowest velocities still present in the beam because of expected deviations from the Maxwell-Boltzmann distribution due to the Zacharias effect. We assume that $v_s = 5.0$ m/s ($v_i \approx 3.8$ m/s) atoms are available from a cryogenic nozzle, corresponding to a deflection angle of $\theta = 41^\circ$. We use these numbers for the discussion in this work even though the final design may differ.

The deflected atoms are funneled (curved lines) by the 515-nm trapping laser dipole force towards the high-intensity trapping region, where they are predominately quenched to the $1S$ ground state. This happens because the trapping laser mixes the metastable $2S$ state with the short-lived P states, causing the $2S$ state to decay. The quenching process is described in more details in Sec. VI A. This gives rise to a large recoil from the involved photons in a random direction and changes the velocity by as much as 4 m/s. Without this kinetic energy dissipation, atoms that enter the trap would exit on the other side. This process ensures that dissipation occurs predominantly within the trap region, reducing unnecessary dissipation in areas where it would be ineffective. A fraction of the atoms receive the proper recoil to let them stay in the trap (see Sec. VI B), and a steady number of trapped atoms develops from the equilibrium of the trapping and loss rates (discussion in Sec. VI E). The loss rate is dominated by collisions of trapped atoms with the background gas rather than from the incoming atomic beam as described in Sec. VI D.

Loading a shallow trap with a low intrinsic quenching rate might be possible with an additional quenching laser close to the Balmer-α $2S$-$3P$ transition at 656 nm. The fast decay of the $3P$ state to the ground state can provide the required recoil. By blue detuning this laser, an additional potential barrier can be generated that slows down the atoms before quenching them. As the $2S$-$3P$ transition is dipole allowed, milliwatts power level would be sufficient for this purpose, which is readily available from a diode laser. Even though a shallow trap would significantly reduce the experimental efforts and many important systematic effects, it also reduces the loading rate because fewer atoms get funneled into the trap center.

Energetically, a single 515-nm photon is insufficient to ionize the $2S$ state. However, at high intensities, two-photon ionization is not negligible [60,61]. In this case, the quenching rate competes with the two-photon ionization rate. The former is proportional to the intensity, while the latter is proportional to the intensity squared. Limiting the trapping laser intensity allows for a useful trapping rate while keeping the two-photon ionization rate sufficiently low.

Once the trap is filled, the atomic beam can be turned off by switching off the 243-nm laser. An in-trap cooling step, discussed in Sec. VI F, might be added to reduce the temperature if the second-order Doppler shift is limiting. Note that the $1S$-$2S$ clock transition will be driven as a first-order Doppler-free two-photon transition that does not require a very low temperature. The $1S$-$2S$ clock transition can then be driven with the same 243-nm laser that provides the atomic beam deflection. In the simplest case, the signal for a successful $1S$-$2S$ transition would be subsequent ionization possible with a third 243-nm photon (see Sec. VII A). Ions can be detected with a quantum efficiency close to unity and a very low background. In Sec. VII C, we discuss the expected uncertainties of the optical hydrogen clock.

Even without trapping, the velocity selective deflection method can potentially enhance current experiments on atomic hydrogen by generating a cold atomic beam. At present, precision spectroscopy of atomic hydrogen relies heavily on thermal atomic beams [54,57]. However, the accuracy of these measurements is limited by factors such as the Doppler effects and other systematic errors associated with the motion of the atoms. Efforts are made to minimize these limitations [62–64].

III. CRYOGENIC NOZZLE

Atomic hydrogen is produced in a McCarroll-type discharge radio frequency cavity [65] and guided to the cryogenic nozzle with Teflon tubing that is known to prevent recombination to molecular hydrogen [66]. We previously estimated the flux of atomic hydrogen emanating from one side of our T-shaped nozzle to 1.6×10^{16} atoms per second [56] by using the flux of molecules into the radio frequency discharge and an estimated dissociation fraction of 10%. Most of the molecular hydrogen freezes at the nozzle such that the emerging gas has about the same particle flux of atomic and molecular hydrogen. Based on the result presented in Ref. [57], we know that the flux from a "bent nozzle" can be considerably higher. A flux of up to 10^{20} atoms per second has been reported in the literature [67]. As we have not yet fully characterized other designs, we estimate that we will be able to generate a flux of $f_0 = 10^{18}$ atoms per second. Molecular hydrogen freezing at the nozzle orifice may limit the uptime of the experiment. A large flux is a key element in this proposal because it permits us to select a tiny fraction of trapable atoms from it while still having a sufficient signal-to-noise ratio.

As a first approximation, we assume the Maxwell-Boltzmann velocity distribution for an effusive beam. This distribution is multiplied by the velocity v to obtain the flux

as a function of the magnitude of the velocity [68,69]

$$f(v)dv = \frac{2v^3}{v_0^4}\, e^{-(v/v_0)^2} dv \quad \text{with} \quad v_0 = \sqrt{\frac{2k_B T}{m}}, \qquad (1)$$

with the Boltzmann constant k_B, the mass of the atoms m, and the mean (flux averaged) thermal velocity $(3\sqrt{\pi}/4)v_0$. At a temperature of $T = 5$K, we have $v_0 = 287$ m/s for atomic hydrogen.

The low-velocity tail of this distribution is largely suppressed. The flux at $v_s = 5$ m/s atoms that we select (see below) is almost five orders of magnitude lower than the peak of the flux distribution of the ideal Maxwellian. Moreover, for the lowest velocities, the Zacharias effect almost certainly modifies this distribution, which further reduces this number. The nozzle properties have been extensively discussed in Ref. [54]; however, without treatment of this suppression of the slow atoms. How strong this suppression is depends on the shape of the nozzle, the distance from the nozzle, and most likely on other things, as discussed in the following.

A. The "Zacharias effect"

1. Intrabeam

Obtaining a significant fraction of slow atoms is essential for the proposed experiment. The Zacharias effect removes those atoms by collisions within the beam [58,59,70]. An analytic expression that describes the modification of the velocity distribution in a collimated atomic beam at large distances from the nozzle has been derived [71,72], long before J. R. Zacharias attempted the first atomic fountain experiment that failed because of the lack of slow atoms in a thermal beam. To accommodate this effect the Maxwellian in (1) needs to be multiplied with a suppression factor $e^{-v_{\rm cut}/v}$ with $v_{\rm cut} = \sigma r_n \rho_0 v_0/\sqrt{\pi}$ that includes the nozzle orifice radius r_n, the density of atoms and molecules within the nozzle ρ_0, the Bohr radius a_0 and the collisional cross section σ.

The latter requires special attention. It is not simply given through the Bohr radius. Instead, the assumed cross section is defined by the process that deflects an atom by an angle sufficient to remove it from the beam. Hence, it depends on the long-range interaction, the beam shape, and the mean velocity of the atoms. By solving the Newtonian equation of motion in a potential $-C_6/R^6$ with the distance R and the van der Waals coefficient C_6, the deflection radius is obtained as $r_d = (15\pi C_6/16 k_B T)^{1/6}$ [73], which is the minimum distance of a slow atom being passed by a fast atom with an average speed (in the beam) of v_0 and experiences a deflection angle of 45° due to this passage. This angle is the opening angle of the beam leaving the nozzle [see (8)]. The assumption here is that lower deflection angles merely redistribute the slow atoms within the atomic beam, while larger angles lead to their removal. The cross section for slow atom removal is then given as $\sigma = \pi r_d^2$.

Precise values for the van der Waals coefficients for the interaction of a $1S$ hydrogen atom with another one and with a H_2 molecule can be obtained as $C_6 = 6.50 a_0^6 E_h$ and $C_6 = 8.7 a_0^6 E_h$, respectively [74], with the Hatree energy E_h. Using the larger of the two coefficients, we get $\sigma = \pi(11 a_0)^2$. For our previous T-shaped nozzle, we estimate the particle density inside the nozzle to be $\rho_0 = 5.4\times10^{19}$ m^3 [56]. With $r_n = 0.5$ mm and $T = 5$K, we obtain $v_{\rm cut} = 4.7$ m/s (ignoring the lower mean velocity of H_2 in the beam). Figure 3 plots the suppression function under these conditions. This somewhat justifies the assumption that we will have some $v_s = 5$ m/s atoms at our disposal.

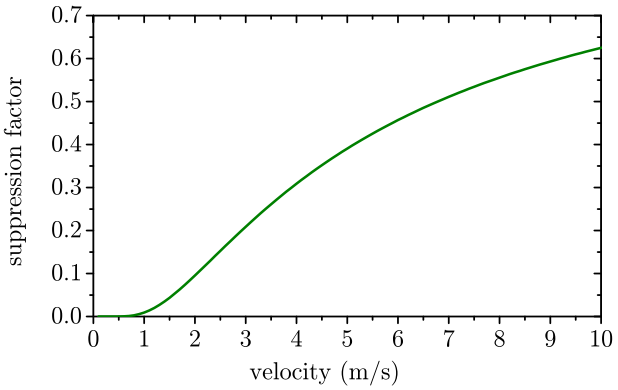

FIG. 3. The "Zacharias" slow velocity suppression factor $e^{-v_{\rm cut}/v}$ for $v_{\rm cut} = 4.7$ m/s that multiplies the Maxwell-Boltzmann distribution based on the theory presented in Ref. [71]. For $v_s = 5$ m/s, the suppression factor is 0.4.

It is crucial to acknowledge that the results of the Zacharias effect are not definitive. Achieving estimates of the Zacharias effect given above necessitates further extensive theoretical work. Such in-depth analysis extends beyond the scope of this paper. Hence, it is essential to recognize the potential for inaccuracies in these initial estimations for this effect. Consequently, an experimental confirmation is desirable at this stage.

2. Intranozzle

The T-shaped nozzle is designed so that its inner surfaces do not intersect the atomic beam axis, meaning all on-axis atoms are generated through atom-atom collisions. As a result, the on-axis beam intensity is reduced compared to the bent nozzle design. Increasing the internal pressure of the T-shaped nozzle augments the collision rate and subsequently boosts the on-axis atomic flux. However, this also leads to a pronounced intrabeam Zacharias effect, lowering the slow atoms flux. In contrast, the bent nozzle design can operate effectively at lower pressures, achieving comparable flow rates while preserving the slow atom component. Consequently, the flux from the nozzle has a scalability limit, and increasing the pressure indefinitely is not a viable solution to enhance the slow atom flux.

The reduction of the total flux and the suppression of the slow atoms from a T-shaped nozzle have been clearly observed earlier [57]. The same work also shows data for a bent nozzle. In this configuration, the atoms forming the atomic beam emerge directly from a cold surface within the nozzle, not from collisions. Such a nozzle does not show any measurable suppression of the slow atoms, albeit the detection limit due to the apparatus has been $v > 78$ m/s [57]. Moreover, the flux of the bent nozzle seems to be larger as the signal shows no sign of noise.

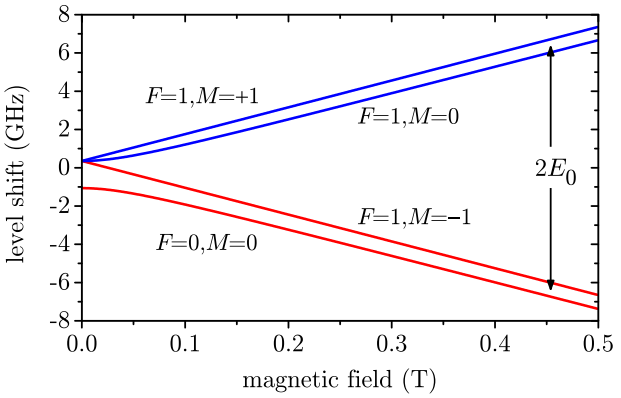

FIG. 4. Breit-Rabi diagram of the hydrogen 1*S* hyperfine levels with total atomic angular momentum F and z component M (the 2*S* looks the same with different splittings). The two lower levels (red) are high-field seekers, while the upper two (blue) are low-field seekers. This property can slow down the high-field-seeking atoms as they leave the nozzle.

Independently, we can also confirm this problem of the T-shaped nozzle using the delayed detection scheme in Ref. [56]. In contrast to the intrabeam model of I. Estermann and O. Stern [71], we find a very different temperature dependence [56]. We explain this with the strong temperature dependence of the recombination rate (atomic hydrogen to molecular hydrogen), which is not part of the Estermann model. With the nozzle design sketched in Fig. 2, atoms that emerge from a cold surface form the beam that is velocity selected. Hence, we expect the intranozzle Zacharias effect will be significantly decreased in this design.

B. Magnetic slowing

To further enhance the flux of slow atoms, we plan to include a strong permanent magnet into the nozzle as sketched in Fig. 2. The magnetic interaction energy of the high-field-seeking atoms is dominated by the electron's magnetic moment in the Paschen-Back regime. This energy is given by the larger splitting at the high field side of the Breit-Rabi diagram [75] shown in Fig. 4. The velocity flux distribution (1) of the high-field-seeking atoms is shifted towards lower velocities via

$$\frac{mv_i^2}{2} \to \frac{mv_f^2}{2} + E_0, \tag{2}$$

as these atoms leave the nozzle. Here $E_0 = -\mu_B B$ with Bohr's magneton μ_B and the magnetic field B at the surface.

In this way, we derive a modified flux distribution of velocity magnitudes v

$$f_m(v)dv = \frac{2(v^2 + 2E_0/m)^{3/2}\, e^{-v^2/v_0^2}}{\sqrt{\pi}\, v_0^4 U(-3/2, -1, E_0/k_B T)}\, dv, \tag{3}$$

with the Tricomi confluent hypergeometric function $U(a, b, z)$ in the normalization factor. The distribution for the low-field-seeking atoms has the sign of E_0 flipped. Figure 5 plots these distributions for magnetic field maxima of $B = 1$ T and $B = 10$ T. The relative enhancement of the slow atoms is also shown. According to this model, the flux enhancement at

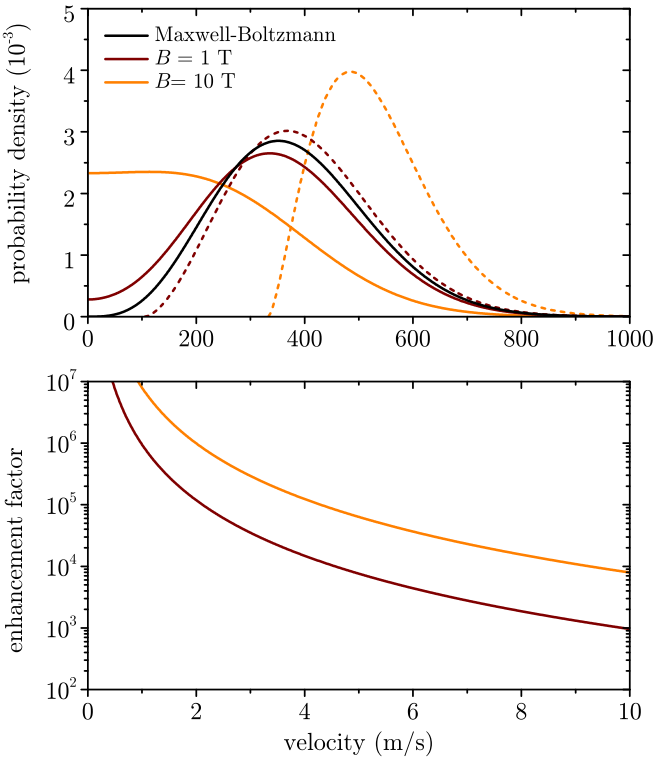

FIG. 5. Top: Maxwell-Boltzmann distribution (black) according to (1) and modification by a magnetic field $B = 1$ T and $B = 10$ T according to (3). The dashed curves represent the corresponding low-field-seeking atoms that get accelerated upon leaving the nozzle. Bottom: Ratio of the modified velocity distributions of the high-field-seeking atoms normalized to the unmodified Maxwell-Boltzmann distribution in the range of low velocities for $B = 1$ T and $B = 10$ T.

$v_s = 5$ m/s is 8×10^3 with a magnetic field maximum of $B = 1$ T and gets significantly larger for lower velocities. Increasing the magnetic field strength to 10 T would result in another order of magnitude improvement.

A magnetic field of 1 T can be generated by a permanent magnet with a conic shape where the poles are at the tip and base of the cone (see Fig. 2). Due to the focusing of the magnetic field lines at the tip, one can get the highest magnetic field amplitude using this configuration. Permanent magnets lose some of their magnetization at cryogenic temperatures [76]; however, NdFeB magnets tend to lose no more than 15%. The magnetic field created by a permanent magnet with a cone shape has rotational symmetry around the axis. As explained in Sec. V A, high-field-seeking atoms will be focused toward the axis. The same effect will also deflect the low-field-seeking atoms away from the axis, possibly reducing the intrabeam Zacharias effect due to asymmetry in the velocity distribution. The details depend on the exact shape of the magnetic field. As long as the atoms leave the nozzle mostly as a forward-directed beam, the reorientation of the velocity vector should not be the dominating effect. We ignore any associated focusing or defocusing.

Higher magnetic fields, on the order of a few tesla, can be achieved using superconducting magnets incorporated into the nozzle. Even though the nozzle is cooled to 5 K, including such an electromagnet is complicated, and even a field of 10 T

would gain only one order of magnitude improvement. We are not planning to use larger fields at this stage.

The escape velocity from the magnetic surface is $v_e = \sqrt{2\mu_B B/m} = 105$ m/s. By integrating (1) from $v = 0$ to $v = v_e$, we conclude that the total atomic flux from the nozzle will decrease by a negligible amount of 0.8%.

Due to the hyperfine splitting, we can only address one-quarter of the atoms coming out of the nozzle with the deflection beam discussed next. Addressing both high-field-seeking states, $F = 0$, $M = 0$, and $F = 1$, $M = -1$, would require a second laser frequency, further complicating the experiment.

IV. BEAM DEFLECTION

After the nozzle, the atomic beam crosses a $\lambda = 243$-nm laser beam at an angle θ_0 as sketched in Fig. 2. We assume that the geometry is arranged such that the deflection laser crosses the trapping laser beam axis at a right angle, i.e., $\theta + \theta_0 = 90^\circ$. After absorbing two 243-nm photons, the atoms get excited to the $2S$ state and deflect by an angle

$$\theta = \arcsin(v_r/v_s), \tag{4}$$

where the recoil velocity is $v_r = 2h/(m\lambda) = 3.26$ m/s. The geometry is arranged so the deflected atoms center around the z axis. The recoil shifts the velocity input to the trap:

$$v_i = \sqrt{v_s^2 - v_r^2} \quad \text{for} \quad v_s > v_r. \tag{5}$$

We want to use $v_i = 3.8$ m/s for trapping, that is, the $v_s = 5$ m/s atoms from the nozzle. This implies a deflection angle of $\theta = 41^\circ$.

The deflection laser must be tuned to the Doppler-sensitive $1S$-$2S$ resonance that uses two photons from the negative (positive) x axis. To meet the resonance condition, this laser frequency needs to compensate for the Doppler and recoil shift,

$$\Delta\nu_D = 2v_s \cos(\theta_0)/\lambda = 27\,\text{MHz}, \tag{6}$$

$$\Delta\nu_{\text{rec}} = 2h/(m\lambda^2) = 13.4\ \text{MHz}. \tag{7}$$

To determine the efficiency of the deflection process, we assume the 243-nm laser diameter covers the diameter of the trapping laser at the crossing point. We assume the 243-nm laser has a beam radius of $w \gtrsim r_n = 0.5$ mm along the y direction. Note that the atomic beam does not need to cross the 243-nm laser at the beam waist position. Moreover, we would prefer a small d_n to have a large atomic flux and to reduce the intrabeam Zacharias effect as detailed in Sec. III A. This distance can be reduced to $d_n = 10$ cm.

The deflection efficiency is obtained by solving the optical Bloch equations along the atomic trajectories [77] (see Fig. 18). Figure 6 shows the corresponding numerical solution. The intensity should not be too high to limit ionization. Under the above conditions, the optimum laser power is around 5 W, which can be reached within an enhancement resonator [78,79]. With this power, we obtain a deflection efficiency of $P_{\text{ext}} = 12\%$.

To compute the trapping rate in Sec. VI C 1, we must determine the flux of deflected $2S$ atoms through the trapping region. The flux distribution from the nozzle has a characteristic $\cos(\vartheta)$ distribution around its axis and is given in spherical coordinates [68]:

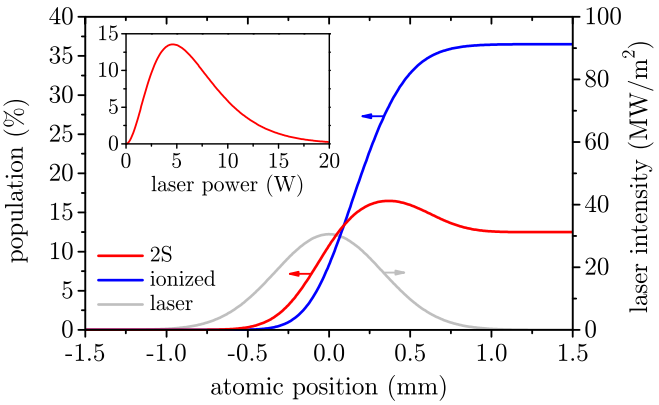

FIG. 6. Solution of the optical Bloch equations for hydrogen atoms moving at $v_s = 5$ m/s across a 5-W, 243-nm laser beam with a waist of $w = 0.5$ mm, intersecting the optical axis at an angle $\theta = 41^\circ$ as shown in Fig. 2. The red and blue curves show the evolution of populations of the $2S$ state and the ionized state, respectively, as a function of position along the atomic trajectory. The time origin $t = 0$ corresponds to a position 1.5 mm upstream from the optical axis. About $P_{\text{ext}} = 12\%$ of the atoms end up in the $2S$ state, receiving a recoil of $v_r = 3.26$ m/s. Thirty-six percent of the incoming atoms get ionized with this setting. The laser detuning was set to compensate for the light shift at the center of the laser beam and the much smaller second-order Doppler shift. This is not exactly the optimum detuning, but quite close. The gray curve sketches the laser intensity (without scale) that peaks at around 31 MW/m^2. The inset shows the final $2S$ occupation, which peaks at a laser power of around 5 W. More laser power would increase the number of ions and reduce the number of deflected atoms.

$$f(\vartheta, \varphi, v)d\vartheta d\varphi dv = \frac{2v^3}{\pi v_0^4} e^{-v^2/v_0^2} \cos(\vartheta)\, \sin(\vartheta) d\vartheta d\varphi dv. \tag{8}$$

Only a small opening angle ϑ_{max}, restricted by the geometry, can be used:

$$\int_0^{2\pi} \int_0^{\vartheta_{\text{max}}} f(v, \varphi, \vartheta)d\vartheta d\varphi = \frac{2v^3}{\pi v_0^4} \sin(\vartheta_{\text{max}})^2\, e^{-v^2/v_0^2} dv. \tag{9}$$

This finite acceptance angle is set by the funneling of the trapping laser, by the nozzle radius, and the distances d_n and d_t. The latter has to accommodate the differential pumping sections.

The remaining integral of (9) extends over the velocity. The time of flight broadening [80] is of the order of a few kHz in the geometry discussed here. So it is ineffective to address a larger fraction of atoms via the Doppler shift (7). Instead a range of incoming angles $\Delta\theta$ addresses a range of incoming velocities Δv_s:

$$\Delta v_s = v_s \tan(\theta)\Delta\theta. \tag{10}$$

With that, we obtain the relative flux of atoms into the trap:

$$F_\Omega = \int_{v_s-\Delta v_s}^{v_s+\Delta v_s} \frac{2v^3}{\pi v_0^4} \sin(\vartheta_{\max})^2 \, e^{-v^2/v_0^2} dv \approx \frac{4v_s^3}{\pi v_0^4} \sin(\vartheta_{\max})^2 e^{-v_s^2/v_0^2} \Delta v_s. \quad (11)$$

V. TRANSPORT

Once the 243-nm laser beam has deflected the atoms, we expect to obtain a beam with a very narrow velocity distribution. If the apparatus is oriented vertically, then the beam travels a distance $d_t = 30$ cm against gravity as seen in Fig. 2, such that the final velocity is given by:

$$v_{d_t} = \sqrt{v_i^2 - 2gd_t}. \quad (12)$$

An atom with an input velocity of 3.8 m/s would be slowed down to 2.9 m/s without the potential of the trap.

A velocity-selected beam of metastable hydrogen could also be very interesting for other future spectroscopy experiments. The introduction of the first cryogenic hydrogen beam [54] has greatly improved the precision of the measurement. Further cooling of the atomic beam is expected to improve the precision even further, especially for single-photon transitions for which the Doppler effect remains a challenge [62,63]. While the beam described here is not being cooled (no energy is extracted from the system), the velocity distribution is narrow due to spatial filtering. If we associate it with $\overline{v^2} - \overline{v}^2$ from a three-dimensional Maxwell-Boltzmann distribution, then we obtain a corresponding temperature of:

$$T \approx \frac{\pi m}{k_B(3\pi - 8)} \Delta v^2. \quad (13)$$

Using this relation, for the longitudinal velocity spread of $\Delta v_s \approx 0.1$ m/s, the characteristic temperature is $\approx 3\,\mu$K. This number expresses the potential of the velocity selector and should not be attached to any thermodynamic meaning.

A. Magnetic focusing

A hydrogen atom experiences a force due to the interaction between a magnetic field gradient and its magnetic dipole moment [81]:

$$\vec{F} = \pm \mu_B \vec{\nabla} |\vec{B}|. \quad (14)$$

The magnitude of the magnetic field acts as a potential so that the force is conservative. In an adiabatic quantum mechanical situation, we have either a high-field or low-field-seeking state (see Fig. 4). The single electron of the ground-state hydrogen atom dominates the magnetic moment in (14).

An atom that passes through a spatially constant magnetic field gradient perpendicular to the initial velocity of the atom experiences an angular deflection. This deflection angle is proportional to the time of flight through the magnetic field gradient and, hence, inversely proportional to the velocity. A rotational symmetric magnetic field magnitude is used to focus an atomic beam. Such a field may be obtained with a single coil, an anti-Helmholz coil pair, or a hexapole magnet. Focusing takes place when the magnetic field gradient grows linearly from the axis. The situation is exactly as in paraxial optics, and the ABCD matrices can be used, except that the focal length has a quadratic dependence on the longitudinal velocity v. As an example, a hexapole magnet with a radius R and length d that is carrying a current of I makes a lens with a focal length [82]

$$f = \frac{\pi m R^3}{6\mu_0 \mu_B I d} v^2. \quad (15)$$

For $R = 3$ cm, $d = 2$ cm, and $I = 25$ A, we get $f = 335$ m for $v = v_0 = 287$ m/s and $f = 10$ cm for $v = 5$ m/s. The fast atoms essentially see no lens at all, while the slow atoms focus at a reasonable distance. Such a lens could be included between the nozzle and the deflection laser to increase the flux into the trap.

The selection rules of two-photon transition between two S states forbid $\Delta M \neq 0$ and $\Delta F \neq 0$ transitions [83]. This implies that the deflection laser can only excite atoms from a high-field-seeking state into another high-field-seeking state. To transfer atoms to a low-field-seeking state, which can be focused using a magnetic lens [84], an extra spin-flip microwave cavity [85,86] is required. However, implementing this could complicate the apparatus.

B. Beam lifetime

1. *Natural lifetime and quenching*

Even though the natural lifetime of the $2S$ state is $\tau_{2S} = 122$ ms, about 48% of the atoms will decay on the way to the trap center with the parameters that we have assumed. A stray electric field will further reduce the lifetime of the $2S$ state by mixing in the short-lived $2P$ state. Using perturbation theory, the reduced lifetime is obtained as ((67.8) in Ref. [87] and Sec. 4.4 in Ref. [88]):

$$\tau_{2S}(E) = \left(\frac{E}{47.5\,\text{kV/m}}\right)^{-2} \tau_{2P} \quad \text{with} \quad \tau_{2P} = 1.6\,\text{ns}. \quad (16)$$

Even a moderate electric field of a few volts per centimeter significantly reduces the lifetime of the $2S$ state. Since the experiment is being done under UHV conditions, the vacuum chamber already shields the atomic beam from stray electric fields. Care must be taken when the atomic beam passes near a surface, as patch charges may develop. This is highly relevant for the differential pumping stage discussed in Sec. VI D. We should be able to avoid most of these effects by making sure the inside of the vacuum chamber is well conducting.

The $2S$ atoms may also be quenched to the $1S$ state by moving through a magnetic field. According to electromagnetism of moving bodies, a moving atom in a magnetic field feels an electric field,

$$\vec{E}_B = \vec{v} \times \vec{B}, \quad (17)$$

where we assume $v \ll c$.

One source for a magnetic field would be the magnetic focusing lens described in Sec. V A. Taking exaggerated values for the magnetic field of 10^{-2} T, the time-of-flight 1 s (much longer compared to the natural lifetime of the $2S$ state), and assuming that the field is uniform and perpendicular to the movement direction of the atom, the population of the $2S$ state

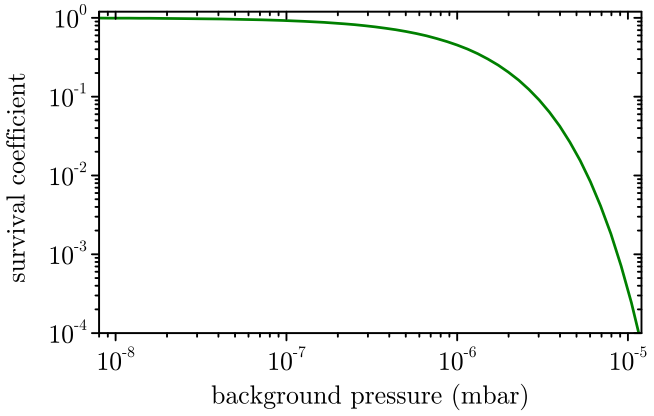

FIG. 7. Survival probability of a $2S$ hydrogen atom traveling 5 cm at 3.8 m/s in a hydrogen background gas at $T = 300$ K. For the $2S$ atoms to reach the trapping area, it is essential to maintain a low pressure of less than 10^{-6} mbar. We assume that the survival coefficient is unity after the first differential pumping stage, where the pressure is on the order of 10^{-8} mbar or lower.

is reduced by 0.08%. Hence, we assume that magnetic fields do not significantly quench the slow $2S$ atomic beam.

2. Collisional lifetime

When colliding with the background gas at pressure P, the $1S$-$2S$ transition becomes broader because the lifetime of the $2S$ state shortens due to collisional quenching. This rate is given by [73]

$$\Gamma_c = 1.29388\,\xi_\gamma^{(6)}\,\frac{P}{m^{3/10}(k_B T)^{7/10}}, \tag{18}$$

where $\xi_\gamma^{(6)} = 3.072(196)\times 10^{-17}$ rad m$^{12/5}$ s$^{-2/5}$ for a collision with a ground-state hydrogen atom. As we do not know the exact ratio of H to H_2 in the background gas, we assume for this consideration that the gas consists solely of hydrogen atoms. This is because the cross section for an atom-atom collision is significantly larger than that of an atom-molecule collision [89]. Using this approximation will provide an upper limit on the lifetime.

After deflection and excitation to the $2S$ state, described in Sec. IV, the atoms travel a distance $L \approx 5$ cm in the high-pressure region before traversing the first differential pumping stage. The survival coefficient of a $2S$ atom traveling at $v_i = 3.8$ m/s is given by $e^{-L\Gamma_c/v}$. We assume that the background gas is thermalized at $T = 300$ K and visualize this relation in Fig. 7. The survival coefficient is 45% for 10^{-6} mbar, assumed for our estimates, and 90% for 10^{-7} mbar. After the atom passes the differential pumping tube, the pressure drops by about three orders of magnitude, and the collisional decay rate becomes negligible.

VI. THE OPTICAL DIPOLE TRAP

The optical dipole trap consists of a focused laser beam (the trapping laser) that shifts the atomic energy levels via the light-induced electric dipole moments. In leading order, the potentials ϕ are given through the electric dipolar $E1$ polarizabilities α of the $1S$ and $2S$ states:

$$\phi^{(1S)}(\vec{r}) = \alpha_t^{(1S)}\, I_t(\vec{r}), \quad \phi^{(2S)}(\vec{r}) = \alpha_t^{(2S)}\, I_t(\vec{r}). \tag{19}$$

Here $I_t(\vec{r})$ is the intensity of the trapping laser. Lengthy but analytic expressions for the coefficients as a function of the laser wavelength are given in Ref. [22].[1] The polarizabilities are wavelength dependent. The trapping laser is set to the magic wavelength [20], where the polarizabilities are negative and identical. For the $1S$-$2S$ clock transition, the longest wavelength that fulfills this criterion has been determined to be 514.646 nm [22] with:

$$\alpha_t = \alpha_t^{(1S)} = \alpha_t^{(2S)} = -2.21584\times 10^{-5}\, h\,\frac{\text{Hz}}{\text{W/m}^2}. \tag{20}$$

To be specific for the simulations that follow, we assume that the trapping laser has a power of $P_t = 1$ kW and waist radius of $w_0 = 50\,\mu$m (peak intensity 2.5×10^{11} W/m^2). The beam radius at the intersection with the deflection beam is 980 μm, which we believe is a good compromise between the beam restrictions for differential pumping and a sufficiently large collection angle. However, the final design might be modified.

The corresponding potential depth ϕ_0 (taken to be positive) is 0.27 mK or 7.5 times the recoil energy of a trap photon. This is a rather shallow trap but comparable to what is employed in the most advanced strontium lattice clocks [90]. For the latter, such potential is achieved with a laser intensity about a factor 200 lower than for hydrogen (factor 25 for the Hg lattice clock [91]). Experimentally, it is desirable to operate at lower powers, which also reduces the main systematic effects and line broadening (see Secs. VII B and VII C). Even though powerful lasers are available at this wavelength as the second harmonic of Yb-based fiber laser systems, it still seems necessary to resonantly enhance the trapping laser light.

To load the trap, we use the velocity-selected metastable $2S$ beam described in the previous sections. As the dipole potential is conservative, we require the atoms to dissipate some energy inside the trap; otherwise, they will leave on the other side. The dissipation is required to be active only while the atom is inside the trap. Usually, this is done with laser cooling, which would be difficult in the case of atomic hydrogen. Instead, we rely on the photon recoil as the atoms are quenched to the ground state through the interaction with the trapping laser. This is possible with a metastable beam and provides just the right amount of dissipation at the right position. This loading mechanism is sketched in Fig. 8.

A. Quenching rate

We now discuss the setting without the additional quenching laser tuned close to the Balmer-α transition (see Fig. 2). There are four paths for quenching with the trapping laser, as

[1]Note that the sign of the hypergeometric function in (3a) in Ref. [22] needs to be reversed.

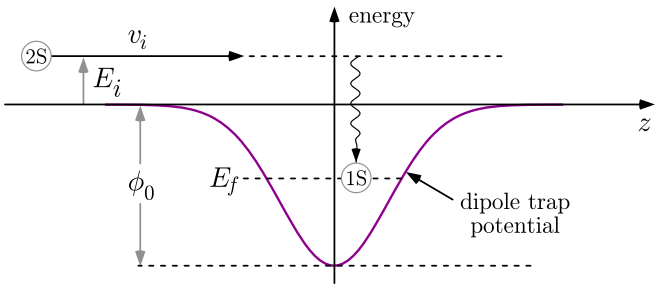

FIG. 8. Schematic of a single recoil trapping. In the $2S$ state, a metastable atom with initial energy $E_i = mv_i^2/2$ rolls into a potential well with constant total energy (upper dashed line). Without dissipation within the trap, the atom would fly out the other side. The trapping laser potential, sketched with the purple line, mixes the metastable $2S$ state with the short lived P levels, causing it to decay ("quench") to the $1S$ ground state. In some cases, the photon recoil slows the atom down, so it will stay in the trap with final total energy $E_f < 0$. This mechanism provides intrinsic overlap between the dissipation and the trapping potential.

sketched in Fig. 9. The rates are linear in intensity and can be computed with equation (D6) in Ref. [77]:[2]

$$\Gamma_a = 1.50\times10^{-9}\,\frac{\mathrm{s}^{-1}}{\mathrm{W/m}^2}\times I_t, \tag{21}$$

$$\Gamma_b = 2.03\times10^{-10}\,\frac{\mathrm{s}^{-1}}{\mathrm{W/m}^2}\times I_t, \tag{22}$$

$$\Gamma_{cS} = 1.14\times10^{-10}\,\frac{\mathrm{s}^{-1}}{\mathrm{W/m}^2}\times I_t, \tag{23}$$

$$\Gamma_{cD} = 9.87\times10^{-12}\,\frac{\mathrm{s}^{-1}}{\mathrm{W/m}^2}\times I_t. \tag{24}$$

We dropped the position dependence of the intensity for simplicity. A value that combined all quenching paths has been published in Ref. [47] and agrees with our values. The dominant quench process (a) involves the absorption of a trapping laser photon and a spontaneous emission of an extreme ultraviolet photon at 98.3 nm. In quench process (b), a trap laser photon is emitted, followed by a spontaneous 159-nm photon. This process is somewhat suppressed due to not having any close resonances. After the absorption of a trapping laser photon in quench process (c), an infrared photon with a wavelength of 2385 nm is emitted as the atom reaches either the $3S$ or $3D$ state. The atom then decays to the $1S$ state via the $2P$ state by emitting a 656-nm Balmer-α photon followed by a 122-nm Lyman-α photon.

B. Favorable recoil fraction

A $2S$ atom that is deflected (launched) at position $\vec{r}_i$ (close to the x axis in Fig. 2) with an initial velocity $\vec{v}_i$ and an initial potential energy $\phi^{(2S)}(\vec{r}_i)$ has a total initial energy of:

$$E_i = \frac{m}{2}\vec{v}_i^{\,2} + \phi^{(2S)}(\vec{r}_i). \tag{25}$$

[2]Note that this equation has an extra factor of 4 and is missing the time-reversed decay paths sketched in gray in Fig. 9. The results presented here are corrected for these issues.

Just before quenching at position $\vec{r}_q$, we can calculate the magnitude of the velocity from the kinetic energy at this point:

$$v(\vec{r}_q) = \sqrt{\frac{2}{m}(E_i - \phi^{(2S)}(\vec{r}_q))}. \tag{26}$$

The quenching event changes the kinetic energy instantaneously, i.e., without changing the position of the atom to

$$E_{\mathrm{kin}}(\vec{r}_q) = \frac{m}{2}(\vec{v}(\vec{r}_q) + \vec{v}_r)^2, \tag{27}$$

with the recoil due to the trapping laser and spontaneous photon $\hbar\vec{k}_l$ and $\hbar\vec{k}_s$ respectively:

$$\vec{v}_r = \pm\frac{\hbar\vec{k}_l}{m} - \frac{\hbar\vec{k}_s}{m}. \tag{28}$$

The sign of the laser photon momentum is positive for quench processes (a) and (c) and negative for quench process (b). The total energy of the atom just after quenching is therefore given by:

$$\begin{aligned} E_f &= E_{\mathrm{kin}}(\vec{r}_q) + \phi^{(1S)}(\vec{r}_q) \\ &= \frac{m}{2}\left(\vec{v}(\vec{r}_q) \pm \frac{\hbar\vec{k}_l}{m} - \frac{\hbar\vec{k}_s}{m}\right)^2 + \phi^{(1S)}(\vec{r}_q). \end{aligned} \tag{29}$$

To evaluate this expression, one may use the Monte Carlo method that randomly selects for the direction of the spontaneous photon(s), that is, for the direction of $\vec{k}_s$. The trapping probability is the fraction of negative values for E_f, while the latter's distribution yields the energy distribution of the trapped atoms. This would be the more complete picture because it readily allows for including quench process (c) with more than one spontaneous photon and nonisotropic dipole emission. The drawback is that it is either slow or not very accurate.

Instead, one may use an incomplete but analytic method. With the trapping laser and spontaneous photon recoil energies $E_l = (\hbar k_l)^2/2m$ and $E_s = (\hbar k_s)^2/2m$ we can rewrite (29)

$$\begin{aligned} E_f &= E_i + E_l + E_s + \Delta\phi(\vec{r}_q) \pm \hbar\vec{k}_l\cdot\vec{v}(\vec{r}_q) \\ &\quad - \hbar\vec{k}_s\cdot\left(\vec{v}(\vec{r}_q) \pm \frac{\hbar}{m}\vec{k}_l\right), \end{aligned} \tag{30}$$

with the potential difference $\Delta\phi(\vec{r}_q) = \phi^{(1S)}(\vec{r}_q) - \phi^{(2S)}(\vec{r}_q)$. The latter vanishes when the trap operates at the magic wavelength. Again, the task is to find the condition for trapping, i.e., when $E_f < 0$. This expression can be written in terms of the angle ε between $\vec{k}_s$ and $\vec{v}(\vec{r}_q) + (\hbar/m)\vec{k}_l$:

$$\begin{aligned} E_f &= E_i + E_l + E_s + \Delta\phi(\vec{r}_q) \pm \hbar\vec{k}_l\cdot\vec{v}(\vec{r}_q) \\ &\quad - \hbar k_s\left|\vec{v}(\vec{r}_q) \pm \frac{\hbar}{m}\vec{k}_l\right|\cos(\varepsilon). \end{aligned} \tag{31}$$

This gives a condition on ε for $E_f < 0$. Assuming an isotropic distribution of ε, we obtain the fraction of recoils that lead to trapping:

$$P_\varepsilon = \frac{1}{2} - \frac{E_i + E_l + E_s + \Delta\phi(\vec{r}_q) \pm \hbar\vec{k}_l\cdot\vec{v}(\vec{r}_q)}{2\hbar k_s|\vec{v}(\vec{r}_q) \pm (\hbar/m)\vec{k}_l|}. \tag{32}$$

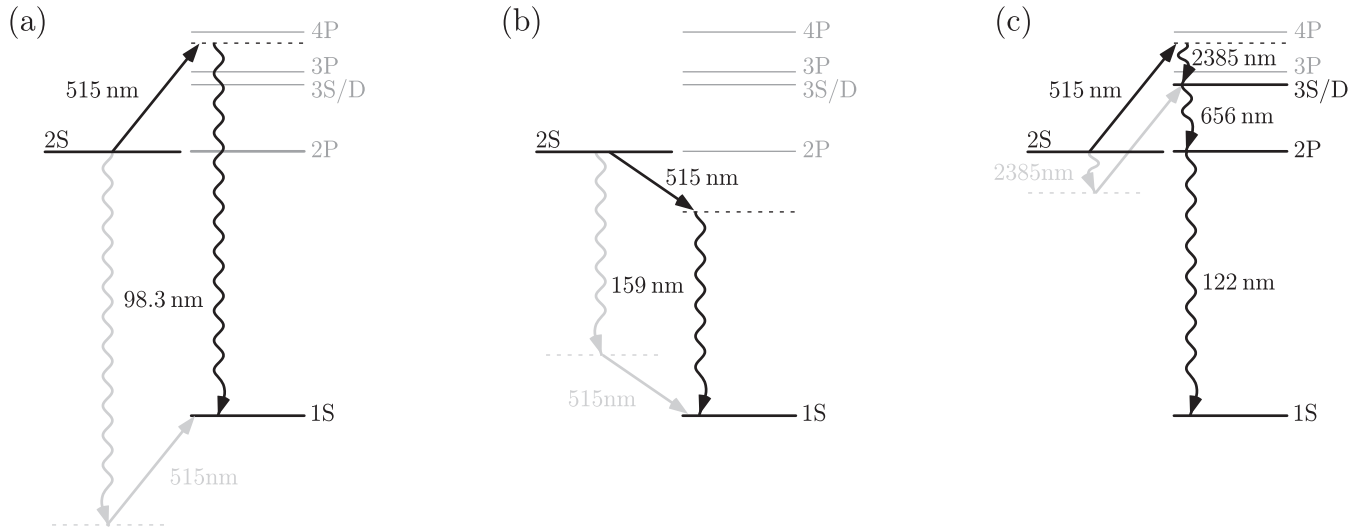

FIG. 9. Decay paths that lead to "quenching" of the $2S$ state due to the trapping laser at 515 nm. In quench processes (a) and (c), the trapping laser excites the $2S$ atoms to a virtual state (dashed) that decays to the $1S$ ground state by spontaneously emitting one or more photons. Quench process (c) can be split into two separate processes, with different rates, where the intermediate states are $3S$ or $3D$. These processes are completed with the time-reversed path via other virtual states (shown in gray) that are below the ground state for (a). In quench process (b), the trapping laser induces a stimulated photon first, which causes the recoil $\hbar\vec{k}_l$ to flip sign in (28). The back decay to the $2S$ state can be ignored here since this process does not lead to quenching (see Sec. VI D 2 for more details). Note that the spontaneous photons (wavy lines) can only point down, whereas the laser photons (straight lines) can point up and down.

Using π-polarized trapping light leads to a nonisotropic distribution of ε, which can enhance the favorable recoil fraction by up to a factor of three. However, this enhancement applies only to very shallow trapping potentials and to atoms propagating along the z axis. For the purposes of our estimation, we adopt a more conservative assumption of an isotropic ε distribution. For process (b), the trapping laser stimulates the emission of a photon, flipping the sign of $\vec{k}_l$ relative to the other processes. The fraction of favorable recoils is plotted in Fig. 10 as a function of the input velocity for an ideal trajectory.

It may be surprising that the counterpropagating trapping laser leads to a lower fraction of favorable recoils for low v_i. However, it should be noted that a lower velocity before the spontaneous emission does not necessarily lead to a larger fraction. In the extreme case, an atom at rest in the trap center before the emission of a high-energy photon will always be ejected irrespective of the direction of this photon. It should also be noted that larger trapping laser intensities lead to larger cut-off velocities. The trap depth we have chosen for this example is as low as possible but still has a useful trapping probability.

A possible way to increase the trapping probability and allow efficient trapping of higher velocities is to operate the trapping laser at a nonmagic wavelength. Of course the deviation from the magic wavelength can be tolerated only during loading. The atoms must be transferred to a magic wavelength trap for the subsequent clock operation. In this situation, the $2S$ atoms reaching the trap center do not accelerate as described above; instead, they are slowed down as they climb the potential hill. Once at the top of the hill, the chances for a quench event are maximized. This dynamics is similar to the well-known Sisyphus cooling [92]. A similar scheme uses the Zeeman shift instead of the light shift to load an optical dipole trap and achieve Bose-Einstein condensation, all without laser cooling [93]. With the envisioned trapping laser parameters, a $2S$ atom entering with $v_i = 3.8$ m/s along the z axis would

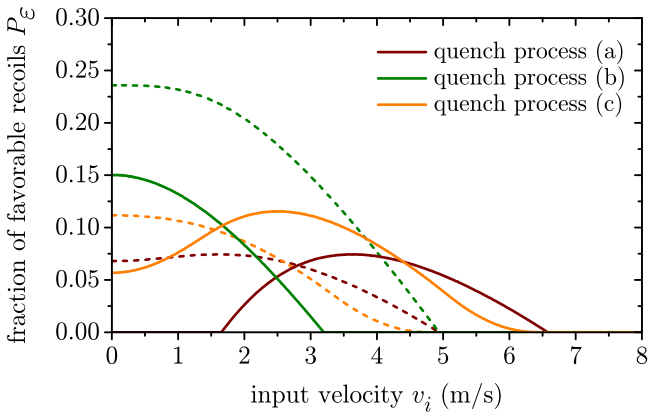

FIG. 10. Fraction of favorable recoils for atoms that quench at the trap center with a trajectory along the z axis starting at infinity with velocity v_i (see Fig. 2). The trapping laser is assumed to be a traveling wave counter- (solid) or copropagating (dashed) with the atomic beam, tuned to the magic wavelengths with a power of $P_t = 1$ kW and a waist radius of $w_0 = 50\,\mu$m. Three quenching processes, (a), (b), and (c), are distinguished (see Fig. 9). The favorable recoils for (a) and (b) are equally well described by (29) and (30) while for (c) it is determined with a Monte Carlo method using (29). Note that the quench path with the largest rate (a) is not necessarily the one with the largest fraction of favorable recoils. Process (b) does not contribute to this particular trajectory with the given conditions, but process (a), with the largest rate, peaks at the chosen input velocity. These curves reach larger values and cut-off velocities with larger laser intensives. However, this leads to a larger ionization rate and not necessarily a larger trapping probability.

be stopped at the trap center if the trapping laser would be tuned to 518.818 nm, i.e., only 4.2 nm away from the magic wavelength.

However, for the suggested geometry such "Sisyphus trapping" would be helpful only for atoms that fly exactly on-axis. The corresponding repulsive force deflects atoms not heading toward the trap center. Hence, we would lose the funneling action of the trapping laser, which reduces the overall loading efficiency. A way around this would be to use a weak knife-shaped laser beam close but blue detuned from the Balmer-α 2S-3P transition as sketched in Fig. 2. This is further discussed in the next section.

C. Single recoil trapping

We solve the Newtonian equation of motion along with the optical Bloch equations for an initial $2S$ state with the potential in (19). For each point along the resulting trajectory, the trapping and ionization probability is computed from the instantaneous velocity and the atom's internal state, which gives the quenching probability. As shown later, the trapping probability is almost three orders of magnitude lower than the fraction of favorable recoils. Integrating over many trajectories gives the total trapping rate, the distribution of quenching positions, and the distribution of the energy of the trapped atoms.

To simulate the trapping dynamics, a set of decay constants in addition to the quenching rates [(21)–(24)] is required. These constants can be computed with almost arbitrary accuracy for atomic hydrogen.

Even though one photon from the trapping laser does not provide enough energy to reach the continuum from the $2S$ state ($\lambda < 356$ nm required), two-photon ionization of the $2S$ state is significant at high intensity with a rate of [60,61,94]:

$$\Gamma_{i,2S} = 2.83\times10^{-20}\,\frac{\mathrm{s}^{-1}}{\mathrm{W}^2/\mathrm{m}^4}\times I_t^2. \tag{33}$$

As the two-photon ionization affects only the $2S$ state, it strongly impacts the trapping procedure but does not limit the trap lifetime once the atoms are in the ground state. However, it broadens the $1S$-$2S$ clock transition by reducing the lifetime of the excited state [47]. Since this rate is quadratic in intensity, it may be reduced relative to the trap depth (see Sec. VII for a discussion).

The natural (two-photon) decay of the $2S$ state has a rate of [95]:

$$\Gamma_{2S} = 8.229062\ \mathrm{s}^{-1}. \tag{34}$$

However, the trapping process discussed in this work may take $\approx$100 ms so that it becomes comparable to the natural lifetime $1/\Gamma_{2S}$ of the $2S$ state. We assume that atoms that decay via the natural decay path are lost and cannot be trapped.

1. Monte Carlo simulation of atom capturing

With the quasitemperature given in (13) and the parameters used in this proposal, the thermal de Broglie wavelength is around 1 μm. The atoms are sufficiently localized for a traveling-wave trapping laser beam to be treated with classical trajectories for the required accuracy. We may expect some quantum corrections to the trapping probability with a standing wave laser. Another source of delocalization would be superpositions where the ground and the excited states separate by a photon recoil (see discussion in Ref. [96]). However, superpositions of this type do not occur in the modeling of the loading procedure described here.

After the atoms are deflected by absorbing two 243-nm photons, some of them are guided by the trapping laser until they absorb or emit a directed photon recoil momentum $\hbar\vec{k}_l$ from that laser. This recoil is followed by one of the spontaneous processes sketched in Fig. 9. Some of those recoils lead to trapping. The main advantage of the classical trajectory is that the recoils can readily be included in a Monte Carlo method. For this purpose, a numerical solution of the Newtonian trajectory with the potentials given in (19) is generated. In each time step, the trapping probability is determined either by (32) for processes (a) and (b) or by randomly selecting one or three recoils that make up $\hbar\vec{k}_s$ to include process (c) in (29). For completeness, we use the latter method. This is continued for all time steps of the given trajectory to determine its overall trapping probability. A full Monte Carlo simulation is then performed by averaging many trajectories drawn from the distribution (8) and averaging over the initial positions within the nozzle orifice.

We investigate two settings where a traveling-wave trapping laser propagates in the negative z direction, both with and without the quenching laser. We assume the trapping laser to be tuned to the magic wavelength with a power of $P_t = 1$ kW and a waist radius of $w_0 = 50\,\mu$m. The distance from the trap center is assumed to be $d_t = 30$ cm which implies a radius of the trapping laser funnel at the origin of $w(d_t) = w_0\sqrt{1+(d_t/z_R)^2} = 985\,\mu$m (see Fig. 2 for the geometry). This is the setting that we currently envision.

The second setting includes the quenching laser with an intensity of $I_{0q} = 10^4$ W/m^2 blue detuned from the $2S$–$3P$ transition by $\delta = +1$ GHz and with a beam radius of $w_{0q} = 50\,\mu$m. The laser is a traveling wave along the x direction. This requires only a moderate power of 25 μW if only the cross section of the trapping laser is covered. For an easier alignment, using a much larger beam radius in the perpendicular direction ("knife" shape) with a larger power requirement would be advisable. With the quenching laser present, another photon recoil must be considered. In this setting, the power of the 515-nm trapping laser is reduced to 100 W. All other parameters are identical to the first setting. More details and the rest of the required parameters to run the Monte Carlo simulations are given in Appendix A 1.

To estimate the acceptance angle of the funnel provided by the trapping laser, we simulate a set of trajectories in the x-z plane with different input angles. The result of Fig. 11 shows that an upper limit of the acceptance angle is $\vartheta_{\max} \approx 1.5^\circ$ for the setting with the strong trapping laser and without the quenching laser. The limiting case is a pointlike source of atoms right on the axis of the trapping laser. The funneling radius is roughly given by the radius of the trapping laser (about 1 mm) at the launch point, i.e., the intersection with the deflection laser. Moving the source off the center reduces the acceptance angle. The setting with the lower trapping laser power and the quenching laser experiences a reduction of the maximum acceptance angle by about a factor of 3, which

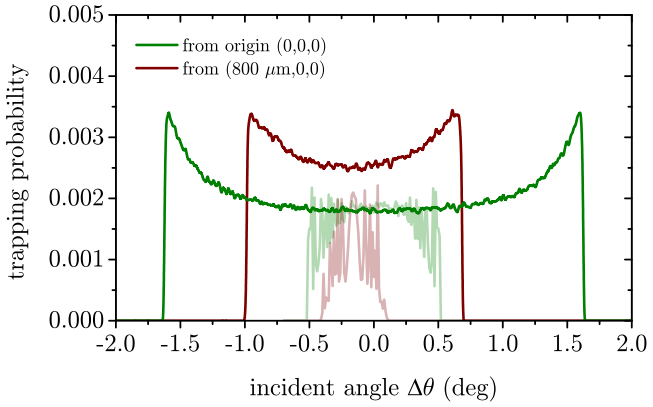

FIG. 11. Monte Carlo simulation to determine the trapping probability. The atoms are launched with $v_i = 3.8$ m/s from the origin $(0, 0, 0)$ (green) and from a point displaced by $\Delta x = 800\,\mu$m $(800\,\mu\text{m}, 0, 0)$ (red) at different angles $\Delta\theta$ using the coordinates system in Fig. 2. The solid curves correspond to $P_t = 1$ kW without the quenching laser and the light curves to $P_t = 100$ W with the quenching laser present. Each of the 200 data points of each curve in this plot belongs to a single Newtonian trajectory along which the trapping probability is determined with 10^6 atoms. The oscillations seen in the light curves are not caused by numerical noise. Rather, they are caused by a well-defined quenching point combined with the oscillatory motion of the atoms as they funnel into the trap. Because of the rotational symmetry, the same conclusion can be drawn for an angle in the y/z plane.

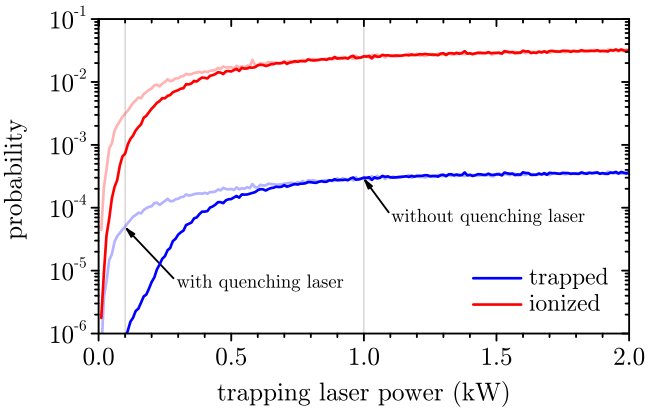

FIG. 12. A full Monte Carlo simulation was performed to determine the trapping and ionization probabilities. This simulation used 10^4 trajectories, each of which was discretized with an average of 10^4 points (with an adaptive step size). Additionally, 10^4 random photon momenta were employed to determine the trapping probability at each of these points. The selected initial velocity is $v_i = 3.8$ m/s. The solid curves correspond to $P_t = 1$ kW without the quenching laser and the light curves to $P_t = 100$ W with the quenching laser present. The trapping probabilities relative to the chosen solid angle ϑ^2_{max}, saturate at around 3.0×10^{-4} for large trapping laser powers. Atoms that are neither loaded nor ionized are the ones that miss the funnel. The capture probability does not drop significantly even for very large laser powers because, in this case, quenching occurs prematurely at the fringes of the laser intensity before the atoms ionize. Note that the probabilities in this plot are relative to the fraction of atoms that make it into the chosen solid angle and cannot directly be compared with the ones given in Fig. 11.

reduces the solid angle by about an order of magnitude. The power of the quenching laser seems irrelevant as long as it is around or above the chosen value. In all those cases, the atoms are almost completely quenched before they reach the intensity peak.

To verify that the chosen power levels are reasonable, we ran a full Monte Carlo simulation where we averaged over a set of source points related to the surface of the nozzle orifice as described in Appendix A 1. We draw trajectories from the distribution (8) for each point but with a fixed magnitude $v = v_i = 3.8$ m/s. We further restrict this distribution to $\vartheta_{\text{max}} < 1.5^\circ$ to speed up the simulation. This restricting angle was picked in accordance with the estimated funneling effect in Fig. 11 (solid curves) and the somewhat larger geometrical restriction of $(R_n + w(d_t))/d_n = 0.85^\circ$ with the funnel radius $w(d_t) = 985\,\mu$m at the crossing of the deflection and trapping laser and the nozzle radius $R_n = 0.5$ mm. The actual value of this cut-off angle is irrelevant as long as it includes all trajectories that could be trapped and with a properly normalized trapping probability. The result is shown in Fig. 12 and reveals that the loading rate is well saturated at a trapping laser power of 1 kW. Two-photon ionization of the $2S$ state by the 515-nm trapping laser dominates for all laser powers. Introducing the quenching laser (light curves) does not improve the trapping probability for large trapping laser powers. However, it allows for the reduction of the trapping laser power. Comparing the two settings, it is seen that the second one has almost an order of magnitude lower trapping probability in agreement with Fig. 11. Lower trapping laser intensity is required with the quenching laser present because it would otherwise quickly ionize the $3P$ level with just one photon (see Appendix A 1).

From the same simulations, we determine the quenching positions, trapping positions, and the trapped atoms' energy distribution. These results are shown in Figs. 13, 14, and 15. These figures show only the results for the first configuration without the additional quenching laser. The y axis shows the raw number of counts per bin from a sample of approximately 10^8 events (10^4 trajectories with around 10^4 points each). These plots are not meant to show total trapping probabilities, as in Fig. 12, but rather the spatial and energy distribution.

As expected, Fig. 13 shows that process (a) is the dominating quenching mechanism. Ionized atoms are not shown in this figure. With the lower trapping laser power and the quenching laser present, the contributions of the quenching processes of Fig. 9 are negligible. Instead, the atoms quench and get trapped about one beam radius before the intensity peak of the quenching laser (at $z = 0$) with a width that is also given roughly by the beam radius.

When one examines Fig. 14, it is clear that only quenching event close to the center of the trap leads to trapping. Only processes (a) and (c) lead to trapping as expected from Fig. 10. The large tail, extending to the left in Fig. 13, comprises atoms that prematurely quenched, some due to the natural lifetime and most due to the trapping laser. Using a smaller focus of the trapping laser leads to a more localized quenching position at the expense of a reduction in the capture angle (see Fig. 11).

The random nature of spontaneous emission leads to an energy distribution of the atoms inside the trap, presented in Fig. 15. Our simulation shows the distribution to be

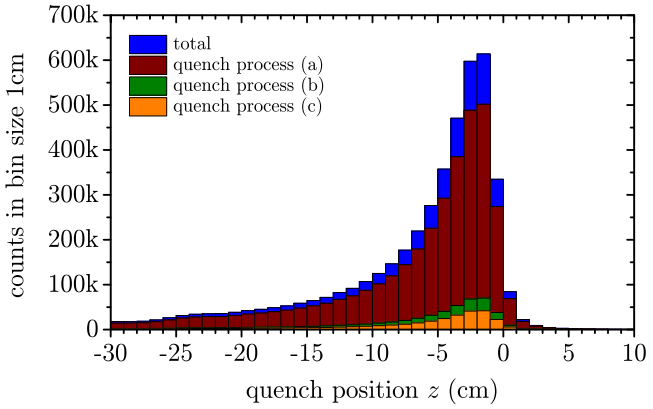

FIG. 13. Same Monte Carlo simulation as in Fig. 12 but with a fixed laser power of $P_t = 1$ kW and without the quenching laser showing the z positions where the atoms are quenched (but not necessarily get trapped). Three quenching processes, (a), (b), and (c), are distinguished (see Fig. 9). The atoms are coming in from the negative z axis. The Rayleigh range of the trapping laser is $z_R = 1.5$ cm. At higher intensities, the atoms are predominantly quenched before reaching the trap's center, where the ionization rate is largest. Premature quenching leads to a higher mean energy (temperature) of the trapped atoms (see Fig. 15) because trapping occurs close to the upper rim of the potential well and away from the trap center. With the quenching laser, this distribution is close to a δ function and is not shown here.

concentrated close to the upper rim of the potential. Since this is not a thermal distribution, temperature is not well defined; however, we could look at a Boltzmann distribution with the same average energy, $\langle E \rangle = 0.77\phi_0 = k_B T$. Such a distribution would have a temperature of 0.21 mK.

We use (11) to determine the relative flux that enters the full Monte Carlo simulation to determine the overall trapping probability. Clearly, $\vartheta_{\max}$ should be the same as in the simulation. In addition, we need to estimate the velocity slice that enters the laser funnel. For this we use (10) and identify $\Delta\theta$ with the acceptance angle, i.e., $\Delta\theta = \vartheta_{\max}$. We use the Monte Carlo simulation to verify this estimation. This gives the span of the deflected atoms around $v_s = 5$ m/s, selected by the deflection, $\Delta v_s = 0.11$ m/s, and the relative flux of $F_\Omega = 1.76\times10^{-12}$. The latter needs to be multiplied by the trapping probability. Note that a larger $\Delta\theta$ would increase the former and reduce the latter.

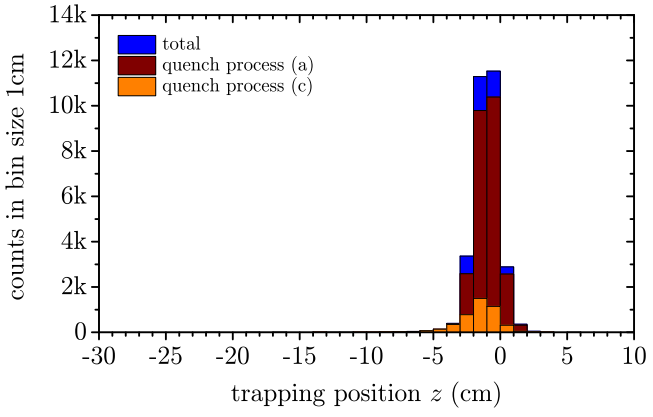

FIG. 14. Same Monte Carlo simulation as in Fig. 13 showing the z positions where the atoms get trapped. With a traveling wave trapping laser, the atoms can move along the z axis roughly within a few Rayleigh ranges of $z_R = 1.5$ cm. With a standing wave trapping laser, we would fill the lattice around 1 cm before the waist. With the quenching laser and reduced power, this distribution is very narrow at about the size of the beam radius of the quenching laser, i.e., 50 μm FWHM in the current case.

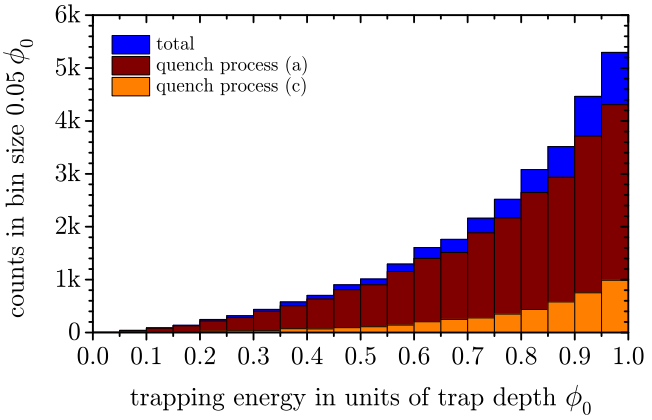

FIG. 15. Same Monte Carlo simulation as in Fig. 13 showing the energies of the trapped atoms in units of the trap depth. While the atoms quench via all three paths (a), (b), and (c) (see Fig. 9), only (a) and (c) contribute to trapping with $v_i = 3.8$ m/s (see Fig. 10). The photon-recoil-assisted trapping places the atoms predominantly at higher energies close to the upper rim of the potential because there is no other dissipation besides quenching of the 2S state. This is more so for higher trapping laser powers because the loading predominantly occurs outside the trap center. Evaporative cooling may occur as discussed in Sec. VI F, removing the higher energetic atoms while reducing the energy of the atomic ensemble, reaching a Boltzmann distribution. Assuming the atom number and average energy of $0.77\phi_0$ remains the same during thermalization, the resulting temperature would be 0.21 mK.

As a third setting we consider a much tighter waist of the trapping laser. This would allow us to dramatically reduce the required trapping laser power while maintaining the intensity and the trap depth. The main issue with this setting is that it reduces the funnel acceptance angle because both the beam divergence increases and the power reduces, as well as the trapping probability for those atoms that get funneled. This prevents loading a large number of atoms into such a tweezer trap [47,97,98] with our loading scheme, at least if one requires a distance $d_t = 30$ cm to fit in the differential pumping section. On the other hand, the idea of the tweezer clock is to have only one atom in the tweezer to reduce collisional shifts. As a specific example, we consider a trapping laser with a 10 times smaller waist radius of $w_0 = 5\,\mu$m and three orders of magnitude lower trapping laser power of $P_t = 1$ W completed with a quenching laser with the parameters of the second setting above. Performing the same simulations, we find that the trapping probability reduces to 1.3×10^{-8}, i.e., by four orders of magnitude relative to the same cut-off angle $\vartheta_{\max}$ for the distribution (8). Even though the acceptance angle of the funnel reduces to about $\Delta\theta \approx 0.005^\circ$ this does not

reduce the addressable velocity slice in (11) because the finite radius of the nozzle allows to compensate the angle mismatch. Hence we expect the tweezer loading rate to be around four orders of magnitude lower than for the first setting. Without the quenching laser, one would require at least $P_t = 10$ W to achieve a comparable loading rate. Unless one finds a way to reduce the distance $d_t = 30$ cm without compromising the differential pumping, this setting may only trap an individual atom at most.

Modeling a standing-wave trapping laser is numerically expensive. However, it describes an important case where the trapping laser is enhanced in a standing wave resonator. We find only small deviations from the traveling wave case by simulating a few representative trajectories within the classical approximation. The moving atoms efficiently average over the nodes and antinodes of the standing wave. With an identical spatially averaged laser intensity, we almost get the same loading dynamics. The only notable difference is that trapping laser photons can be absorbed and emitted in both directions and that the trapped atoms are prevented from moving along the longitudinal trap axis. This localization could be important for evaporative cooling, as discussed in Sec. VI F. Apart from this localization, the standing wave laser may be advantageous as it reduces the required power from the trapping laser. Even with a simple back-reflecting mirror, the spatially averaged intensity doubles.

One may introduce an additional hollow-core guiding laser that runs collinearly with the trapping laser, red-detuned from the magic wavelength to increase the collection efficiency further. This laser could have a tighter waist and a larger funnel opening. Approaching the Balmer-α line at 656 nm from the blue side, the dipole force on the $2S$ atoms could easily be five orders of magnitude larger, which means a few milliwatts of power for the hollow core guiding laser would be sufficient.

D. Trap lifetime

1. Background pressure collision

Trap losses are dominated by the collision of trapped atomic hydrogen with the room-temperature background gas. The trap lifetime is given by [99]

$$\frac{1}{\tau_c} = \left(\frac{450\,\pi^5 C_6^2}{\phi_0 m^3 k_B^4 T^4}\right)^{1/6} \Gamma\left(\frac{11}{6}\right) P_{\mathrm{H}_2}, \tag{35}$$

with the gamma function $\Gamma(11/6) = 0.94\ldots$, the background pressure and temperature of molecular hydrogen P_{H_2} (in pascals) and $T = 300$ K, the trap potential depth ϕ_0 and the van der Waals interactions coefficient $C_6 = 8.7 a_0^6 E_h$ [74]. We assume here that the background gas contains only molecular hydrogen and approximate the mass of a hydrogen molecule to be twice that of a hydrogen atom. Note that while the trap's lifetime depends on the trap depth, the dependency is very weak (sixth root). Equation (35) is plotted in Fig. 16 for the envisioned trap depth using 1 kW.

The nozzle in the first vacuum chamber, as seen in Fig. 2, introduces a large amount of hydrogen into the system. Due to its low mass, H_2 is difficult to pump using turbomolecular pumps. Getter pumps have high pumping speeds for hydrogen; however, they saturate very quickly under heavy gas loads. Achieving a background pressure of less than 10^{-9} mbar is challenging under these conditions. In our previous experiments with a similar setup [8], a background pressure of 10^{-5} mbar was achieved in the beam chamber using a 500 l/s turbomolecular pump. Two stages of differential pumping are implemented in our system as depicted in Fig. 2, each should provide three orders of magnitude reduction in the pressure such that the planned base pressure is 10^{-11} mbar.

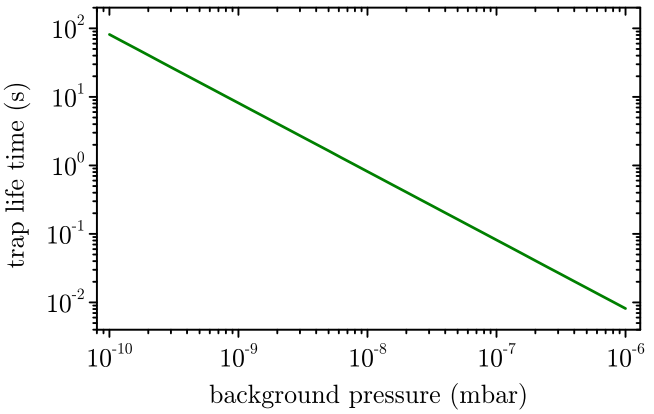

FIG. 16. According to (35), the lifetime of a hydrogen dipole trap with an intensity of 2.5×10^{11} W/m^2 is τ_c. In order to accurately measure the 1.3 Hz linewidth of the $1S$-$2S$ transition, a background pressure of better than 10^{-8} mbar is required.

Even at such a low pressure, the flux from the velocity selected beam, as estimated in Sec. IV, is several orders of magnitude lower than the flux from the background gas as obtained from the flux density of an ideal gas $P/\sqrt{2\pi m k_B T}$. Moreover, the beam comes at a very low velocity and can be shut off by turning off the deflection laser.

2. Rayleigh scattering of trapping laser light

Off-resonance Rayleigh scattering of trapping laser photons leads to the heating of the trapped atoms. We can get an accurate number by realizing that Rayleigh scattering is nothing but the quench rate discussed in Sec. VI A. To compute the scattering rate for the $1S$ ground state, we consider a process similar to Fig. 9(a) with the $2S$ level replaced with the $1S$ level, where the initial and final states are identical. Using the same formalism (see footnote 2), we obtain $\Gamma_a = 2.37\times10^{-13}$ s^{-1}/(W/m^2) which translates to $\Gamma_{\mathrm{Ray}}^{(1S)} = 0.059$ s^{-1}. Along the same line, we can determine the Rayleigh scattering of the $2S$ state through (21). Since Rayleigh scattering and the light shift are described by the same matrix elements, at the magic wavelength the scattering rate for the $1S$ and the $2S$ are identical, $\Gamma_{\mathrm{Ray}}^{(2S)} = \Gamma_{\mathrm{Ray}}^{(1S)}$.

Under the envisioned conditions of the first setting (without the Balmer-α quench laser), a single recoil from the trapping laser increases the energy of a stored atom by $0.13\,\phi_0$. It kicks out only the atoms stored close to the upper rim of the trapping potential (see Fig. 15). The atoms that stay trapped get heated according to $dT/dt = (2E_{\mathrm{rec}})/(3k_B)\Gamma_{\mathrm{Ray}} = 0.7$ μK/s. This is slow enough to provide robust trapping for a sufficient storage time.

TABLE I. The trap gain is given by multiplying the total efficiency with the total initial flux of an estimated $f_0 = 10^{18}$ atoms/s. The trapping probability is given for the first setting of Sec. VI C 1 with a trapping laser of $P_t = 1$ kW with a waist radius of $w_0 = 50\,\mu$m and a selected velocity from the nozzle of $v_s = 5$ m/s. (*) The natural lifetime of the $2S$ state is already included in the full Monte Carlo simulation for F_Ω, so it is left out of the total efficiency.

Trap gain, G		
Channel	Efficiency	Reference
Magnetic slowing	7.6×10^{3}	Figure 5
Zacharias effect	0.4	Figure 3
$1S$-$2S$ excitation	0.12	Section IV
Velocity and solid angle	$F_\Omega = 1.76\times10^{-12}$	Section VI C 1
Hyperfine distribution	0.25	Section III B
Natural lifetime*	0.52	Section V B 1
Collisional lifetime	0.45	Section V B 2
Trapping probability	3.0×10^{-4}	Figure 12
Total efficiency	2×10^{-14}	

Operating the trap with a standing wave, one might expect that photon momenta can be redistributed by stimulated scattering, a process that can lead to Bloch oscillations [100]. However, this process cannot simultaneously obey momentum and energy conservation in a standing wave. Hence, we ignore this type of scattering.

3. Recombination

Atomic hydrogen recombines to molecules at almost all surfaces except liquid helium [101]. Obviously, this problem is absent in an optical dipole trap. However, collisions within the gas may also lead to recombination. The exponential loss of trapped atoms with a time constant of 1.5 s for a 270-mK sample with a density of at least $1.8\times10^{20}/\mathrm{m}^3$ has been measured in Ref. [101]. Expected densities and temperatures here should be considerably lower.

The same work finds an essentially infinite lifetime for a spin-polarized sample like the one planned for our experiment. Spin polarization of the atomic sample can be achieve using σ^--polarized trapping light and using the $F = 1$, $M = -1$ high-field seeking state. This selective decay path confines the population to a single magnetic sublevel. Once established, polarization is preserved by a weak magnetic field, which provides a sufficient quantization axis to prevent mixing between sublevels.

E. Steady-state number of trapped atoms

The steady-state number of trapped atoms depends on the flux through the trap, the trapping probability, and the loss rate from the trap. These factors have been modeled in the preceding sections. The flux through the trap and trapping probability can be combined into a single gain parameter, G. The estimation of this parameter is summarized in Table I. While the total efficiency may be small, we hope to be able to compensate with a large initial flux of atoms.

The steady-state number of atoms in the trap, N, is given by the solution to the rate equation

$$\dot{N}(t) = G - N(t)/\tau_{\mathrm{trap}} \Rightarrow N(t) = G\tau_{\mathrm{trap}}(1 - e^{-t/\tau_{\mathrm{trap}}}). \quad (36)$$

Assuming total flux $f_0 \approx 10^{18}$ atoms/s, the expected gain is $G = 2\times10^4$ atoms/s. The loss rate, $1/\tau_{\mathrm{trap}}$, is estimated in Sec. VI D. From Fig. 16 we read $\tau_{\mathrm{trap}} = \tau_c = 10$ s at a background pressure of 10^{-9} mbar. We conclude that the steady-state number of atoms is on the order of a 2×10^5 atoms after a loading time of about 10 s. This is a typical value for an optical lattice clock. Obviously, the largest reduction factor in the trap gain is the velocity and angular selection given in (11). This is the reason why the funneling action of the trapping laser is essential.

An important enhancement in these estimations is the magnetic slowing inside the nozzle. Further optimization of the parameters used here is conceivable. For example, the number of trapped atoms is inversely proportional to the background pressure, but of course, that also increases the loading time. Employing the quenching laser with a reduced trapping laser power (second setting), we estimate that the loading rate and, therefore, the steady-state trapped atoms reduce by an order of magnitude (see Figs. 11 and 12).

For the tweezer arrangement, as discussed in Sec. VI C 1, we expect to have four orders of magnitude lower loading rate, which reduces the loading rate to about two atoms per second. However, the purpose of the tweezer is to have at most one atom in the trap to avoid collisional shifts, as discussed in Sec. VII C. Meanwhile, large arrays with thousands of tweezers have been demonstrated to compensate for the increased statistical uncertainty [102]. Unfortunately, the hydrogen case would require kilowatts of trapping laser power.

F. Cooling

Even though the $1S$-$2S$ transition is free of the first-order Doppler shift, the second-order Doppler shift might become a limiting factor for subsequent precision spectroscopy. With a trapping laser power of 1 kW and waist radius of $w_0 = 50\,\mu$m, the trapped atoms have a maximum velocity of $v_{\mathrm{max}} = \sqrt{2\phi_0/m} = 2.1$ m/s. This gives rise to a relative SOD shift of $-(1/2)(v_{\mathrm{max}}/c)^2 = -2.5\times10^{-17}$ (see also Sec. VII B). Further cooling may not be required but might take place by itself.

Right after trapping, we expect a distribution of energies as shown in Fig. 15. Thermalization will take place by evaporating the many atoms caught close to the trapping potential's upper rim while reducing the remaining atoms' energy. This initial evaporative cooling [103] will occur even without ramping down the trapping potential. An important quantity is the thermalization time [104]

$$\tau_{\mathrm{th}} = 2^{3/2}(\rho\sigma\bar{v}_r)^{-1}, \quad (37)$$

with the atomic density ρ, the collisional cross section σ, and the average relative speed $\bar{v}_r = 2\sqrt{2/\pi}\,v_0$ [see (1)]. Due to the low atomic density ($\approx5\times10^{14}$ atoms/m^3) and the anomalously small s-wave scattering length of atomic hydrogen ($a_s = 0.4a_0$ for the singlet and $a_t = 1.91a_0$ for the triplet scattering [105]), the thermalization time is on the order of 15 s. This seems impractical for efficient evaporative cooling.

VII. SPECTROSCOPY

A. Detecting the clock transition

The laser to probe the $1S$-$2S$ clock transition (not shown in Fig. 2) could be the same as the 243-nm deflection laser,

although with different requirements. The deflection laser must provide large power but only has moderate linewidth and stability requirements. For the probe laser, the situation is reversed. Nevertheless, employing one laser for both purposes seems feasible when bridging the Doppler shift and recoil detuning of the deflection laser with an acousto-optic modulator. This can be seen as an advantage of the hydrogen clock.

The orientation of the probe laser beam in relation to the trap laser can be configured either collinearly or perpendicularly. A collinear arrangement, where both beams share the same optical axis, presents an experimental challenge, primarily due to the need for an optical cavity that can simultaneously support the trap laser while avoiding residual etaloning of the probe laser. Alternatively, a perpendicular configuration simplifies the cavity requirements but introduces its own complications: To minimize time-of-flight broadening effects, the probe beam must have a sufficiently large diameter [106]. Moreover, this geometry does not take advantage of the strong axial confinement provided by the standing wave of the trap laser.

The simplest method to detect the $1S$-$2S$ transition is to detect protons or electrons generated as the $2S$ state is ionized with a third laser photon at 243 nm. Charged particles can be detected with very good efficiency and low background, for example, with an electron multiplier. Unfortunately, this detection scheme is destructive, so repeated reloading of the trap is required. On the other hand, the proposed scheme allows for continuous loading and probing, potentially avoiding the Dick effect [107] that is present in pulsed atomic clocks. As mentioned in the Introduction, fluctuations of the hydrogen from the nozzle and deflection laser power can be normalized by using the reverse Doppler-sensitive deflected $2S$ atoms. This is essential to suppress noise in a continuous operation mode.

B. Expected line shape

With the current atomic beam experiments [3], the smallest observable linewidth of the $1S$-$2S$ clock transition has been about 1 kHz, i.e., about three orders of magnitude larger than the natural linewidth of 1.3 Hz. We can get closer to this limit or even surpass it with trapped atoms.

The loading mechanism has been described in Sec. VI C by solving the classical Newton's equations of motion. The state of the stored atoms needs to be treated quantum mechanically to understand the details of the observed line shape.

Approximating the potential minimum with a quadratic function, the vibrational frequencies are given by [108]

$$\Omega_t = \frac{1}{L}\sqrt{\frac{2\phi_0}{m}} \tag{38}$$

with the depth of the potential ϕ_0 as treated in Sec. VI and the length scale L. The latter is given by $L = w_0/\sqrt{2}$ for the radial vibration and by $L = \lambda/2\pi$ in the axial direction when a standing wave is employed, resulting in $\Omega_t = 2\pi \times 9.4$ kHz and $\Omega_t = 2\pi \times 4.1$ MHz respectively for our conditions. In the case of a traveling wave trap, the length scale would be the much larger Rayleigh length. Dividing the trap depth by these vibrational frequencies, we obtain the number of supported modes of atomic motion. For our envisioned parameters, this results in about $n \approx 590$ modes radially and $n \approx 10^5$ modes in the axial direction in the case of a traveling wave. Only the axial vibrations for the standing wave case are in the quantum regime with only about $n \approx 1.4$ supported modes.

It is important to note that the Doppler-free two-photon transition makes this situation quite different from the usual optical lattice clocks. No Doppler shift in first order occurs, and the probed atoms do not receive a recoil from the exciting laser. The transitions are limited to $\Delta n = 0$ in first order [47]. It is rather irrelevant whether or not the trap is in the Lamb-Dicke regime and, hence, does not need to be a standing wave lattice.

The second-order Doppler shift, however, leads to a tiny line-shape asymmetry as the vibrational modes impose sidebands only on the red side of the main lines that are shifted by [47]

$$\frac{\Delta f}{f} = -\frac{\hbar\Omega_t}{4mc^2}(2n+1) \tag{39}$$

in relative units. The relative intensity of these sidebands is of the next order in the Lamb-Dicke parameter (see Ref. [47] for details). The second-order asymmetry is obtained through $\hbar\Omega_t n = k_B T$ in the fully thermalized case. With the temperature of the initial sample of 0.21 mK (see Fig. 15), this results in a fractional asymmetry of 9.6×10^{-18}. Therefore, the second-order Doppler sidebands will be covered by the natural linewidth at least.

The observational linewidth is expected to be larger. Two-photon ionization by the trapping laser can severely limit the $2S$ lifetime and broaden the clock transition. With the envisioned trapping laser intensity of $I_t = 2.5\times10^{11}$ W/m^2 and (33) we obtain a linewidth of $\Gamma_{i,2S}/2\pi = 282$ Hz. To mitigate this effect, we may assume that the trapping laser power is reduced after loading or by operating the trap at a lower intensity, as discussed in Sec. VI C 1. Thanks to the quadratic dependence, reducing the laser intensity by one order of magnitude brings the linewidth to the Hz level, i.e., close to the natural linewidth.

Rayleigh scattering and the associated decay through spontaneous photons and atomic recoils may also contribute to the linewidth. As discussed in Sec. VI D 2, the rates are below the Hz level, especially for the reduced trapping laser intensity.

Blackbody-radiation induced width is calculated to be 3×10^{-3} Hz [109] or 1.2×10^{-18} in relative units.

Another line-broadening mechanism is due to power broadening. The resulting linewidth is roughly given by the two-photon Rabi frequency [77]. To reach a hertz-level linewidth, one needs to reduce the intensity of the clock laser accordingly. A hertz-level Rabi frequency is a typical operation mode of an optical clock.

C. Expected clock uncertainties

The main motivation to store atomic hydrogen in a magic wavelength optical trap is to eliminate the systematic uncertainties that dominate the current atomic beam experiments operating at $T \approx 5$ K, namely the light shift and the second-order Doppler shift [3].

Using the mean-squared velocity $\langle v^2\rangle = (3/2)v_0^2 = 3k_BT/m$ of a thermal beam at $T = 5$ K obtained with (1),

the second-order Doppler shift amounts to $-(1/2)\langle v^2\rangle/c^2 \approx 5\times10^{-13}$ in relative units. Typically, one can model this shift within a 1% accuracy to obtain a relative accuracy of around 5×10^{-15}.

With an isotropic Maxwellian distribution of a trapped atomic sample, the mean-squared velocity is given by the same expression but with a much lower temperature. The second-order Doppler shift is roughly given by the second-order Doppler line asymmetry estimated in the previous section to 10^{-17} in relative units. Again, we expect to be able to model this shift within the percentage level to get the second-order Doppler shift under control within a relative uncertainty of 10^{-19}. Additional cooling would further reduce the second-order Doppler shift. Another possibility is to apply a magnetic field (that may also be useful for evaporative cooling) to invoke a motional Stark effect that may partially compensate the second-order Doppler shift [110].

The light shift due to the probe laser is intrinsically large for the two-photon $1S$–$2S$ transition because it is driven off-resonant and requires large laser intensities. The short interrogation time in an atomic beam experiment (on the order of ms) requires even larger laser intensities to excite the atoms. With a probe laser intensity of I_p, the two-photon Rabi frequency is given by $\Omega_R = 2\pi\times7.36222\times10^{-5}$ Hz/(W/m^2) I_p [77]. With trapped atoms, we can set Ω_R to a small value limited by the trap lifetime. With a laser power of 53 μW and a waist radius of 50 μm, the Rabi frequency is about 1 Hz. This results in an light shift of the same order, i.e., 0.36 Hz [77],[3] or a relative shift of 1.5×10^{-16}. Again, there is room for improvements with an even lower probe laser intensity, modeling, and extrapolating to zero probe laser intensity.

With the atoms trapped, we no longer consider the second-order Doppler and the probe light shift the limiting systematic shift. Moreover, the longer interaction time and the small Rabi frequency reduce power broadening. Hence, trapped atomic hydrogen will solve several problems at once.

The two-photon selection rule is $\Delta M = 0$ for any polarization. With the Breit-Rabi formula that was used to generate Fig. 4, one finds the $M = \pm1$ components to be independent of external magnetic fields, at least when the identical Landé g-factors of the $1S$ and $2S$ are used. However, a relativistic correction to the g-factors of $\alpha/3n^2$ (α being the fine-structure constant) leads to a splitting between the $M = +1$ and $M = -1$ components of 37 Hz/Gauss (see the supplement of Ref. [8]). We may pump the atoms into a single Zeeman sublevel or apply a small bias magnetic field to shift the sensitive $M = 0$ out of resonance by employing its quadratic 9.6-kHz/Gauss^2 Zeeman shift. This would require a small magnetic field below 35 mGauss to keep the splitting between the $M = +1$ and $M = -1$ components below the natural linewidth. Stabilization of the magnetic field to 0.1% would then reduce the uncertainty to below 10^{-18}. Employing the motional Stark effect to cancel the second-order Doppler shift [110] does require a much larger field, and hence the $M = +1$ and $M = -1$ components separate and would have to be averaged. The Zeeman effect can be suppressed to much better than the hertz level.

For small fields, the dc Stark shift of the $1S$–$2S$ clock transition is quadratic in the electric field strength E and given by $0.36\,E^2$ Hz (m/V)^2 [55]. It should be possible to shield stray fields to better than 1 V/m [3] and passively reduce the dc Stark shift below the hertz level. We can use the quadratic dependence on the external field to reduce this shift further. The vertex of the parabola describes the observed clock transition frequency as a function of a variable applied electric field, which gives both the unperturbed clock transition frequency and the stray electric field in the direction of the applied field. This method has been used in all three dimensions in the previous beam experiments [8].

The pressure shift of the $1S$-$2S$ clock transition has been determined experimentally at large pressures to $-4.14(36)$ MHz/mbar with a H_2 molecular background gas [111]. A comparable value has been obtained as $-3.8(0.8)\times10^{-16}\rho$ Hz m^3 at lower pressure in an environment of cryogenic spin-polarized atomic hydrogen with a density ρ [112]. We use the former value to estimate the pressure shift in the millihertz regime due to the molecular background gas. Assuming a density of $\rho = 5\times10^{14}$ atoms/m^3 of trapped spin-polarized atoms as in Sec. VI F, we use the latter number to estimate a 10-mHz level collision shift due to the trapped atoms. This shift may be reduced by a larger trapping volume or traded for statistics by reducing the number of trapped atoms. Eventually, trapping in a 3D lattice or a tweezer array could further reduce the collision shift.

The light shift due to the blackbody radiation of the environment has been calculated in Ref. [113] to -1.036 Hz at $T = 300$ K for the hyperfine centroid of the $1S$-$2S$ clock transition. The blackbody shift scales with the total power of the blackbody radiation as T^4, given by the Stefan-Boltzmann law. Knowing the temperature of the environment within 1 K reduces the uncertainty of the blackbody shift of the centroid to 14 mHz. In addition to the centroid shift, the blackbody radiation also couples to the hyperfine splitting. When measuring only one hyperfine component, we are sensitive to both effects. However, the blackbody modification of the hyperfine splitting is at room temperature below the microhertz level [75]. Of course, cooling the environment as it is done in other clocks is another option [114].

In the remaining part of this section, we discuss the lattice shifts induced by the trapping laser through imperfections and higher-order contributions of the light shift. We limit the discussion to an axial probe laser and a standing wave-trapping laser. In this case, the motion of the atoms in the trap has to be described quantum mechanically with a vibrational-state quantum number n not much larger than unity (see Sec. VII B). With the two clock states having slightly different light shifts, the curvatures of the trapping potentials at the minima for these states are no longer exactly equal. This causes the quantized vibrational states within the trapping potential to be modified differently. Approximating the trap potential about the minimum by a quadratic function yields different vibrational-state energies (38) [115]. As a result, the clock transition frequency shifts are not limited to terms linear in the trapping laser intensity I_t as stated in (20). A detailed treatment of the clock transition frequency shift that includes

[3]We measure shifts at the atomic frequency, not at the laser frequency.

the terms under consideration for the most advanced lattice clocks can be found elsewhere [116].

Partial knowledge of this intensity is required to identify such an "operational magic wavelength" [116,117].

As the simplest of these imperfections, the trapping laser frequency may be slightly detuned from the magic wavelength, i.e., $\Delta\nu_t \neq 0$. The slope of the light shift [22] as a function of its wavelengths is similar to other lattice clocks [91]:

$$\frac{\partial\Delta\alpha}{\partial\nu_t} = -2.15748\times10^{-17}\,\frac{\text{Hz}}{\text{Hz W/m}^2}, \tag{40}$$

where $\Delta\alpha = \alpha(2S) - \alpha(1S)$, is the polarizability difference between the two clock states. However, as the hydrogen clock is expected to operate at a larger trap laser intensity, the slope becomes more critical.

For a free atom, the second-order electric dipole perturbation is proportional to the trapping laser intensity I_t while the fourth order is quadratic in the intensity, i.e., $\propto \beta I_t^2$. Note that there are only even orders for the light shift. This higher-order shift is called the hyperpolarizability shift [118]. The real part, i.e., the shift, is given for the $1S$ and $2S$ level by [94]:

$$\begin{aligned}\beta(1S) &= -1.75\times10^{-23}\,\frac{\text{Hz}}{(\text{W/m}^2)^2}\\ \beta(2S) &= -4.88\times10^{-18}\,\frac{\text{Hz}}{(\text{W/m}^2)^2}.\end{aligned} \tag{41}$$

Two more contributions to the light shifts are due to the so-called $E2$ and $M1$ polarizabilities, $\alpha = \alpha^{E1} + \alpha^{M1} + \alpha^{E2}$, where α^{E1} are the same as α_t in (20). Both are linear in I_t and, as such, would merely shift the magic wavelength to a new value if the vibrational frequencies were not modified within the trap. The $E2$ interaction is proportional to the gradient of the electric field of the trapping laser, and $M1$ is proportional to its magnetic field. As the $M1$ matrix elements act only on spins, it can, for the hydrogen $1S$-$2S$ clock transition, only connect hyperfine levels within the same principle quantum number. These are far detuned from the optical frequency of the trapping laser. Hence, the $M1$ induced light shift is very small.[4] We therefore limit the discussion to the $E2$ contribution whose coefficients are given by [94]:

$$\begin{aligned}\alpha^{E2}(1\text{S}) &= -2.52\times10^{-12}\,\frac{\text{Hz}}{\text{W/m}^2}\\ \alpha^{E2}(2\text{S}) &= 3.72\times10^{-9}\,\frac{\text{Hz}}{\text{W/m}^2}.\end{aligned} \tag{42}$$

The light shift generally includes polarization-dependent terms referred to as the vector and tensor polarizabilities distinguished by their rank [118]. Thanks to the scalar character of the $1S$ and $2S$ levels, both terms vanish for the $F = 0 \to F = 0$ transition. A correction due to the tensor light shift must be included if the $F = 1 \to F = 1$ transition is used as the clock transition. The expected tensor light shift must be compared to the smaller Zeeman shift of the $F = 1 \to F = 1$ transition to determine which transition is more suitable for a clock transition. For precision spectroscopy, we would like to measure both transitions.

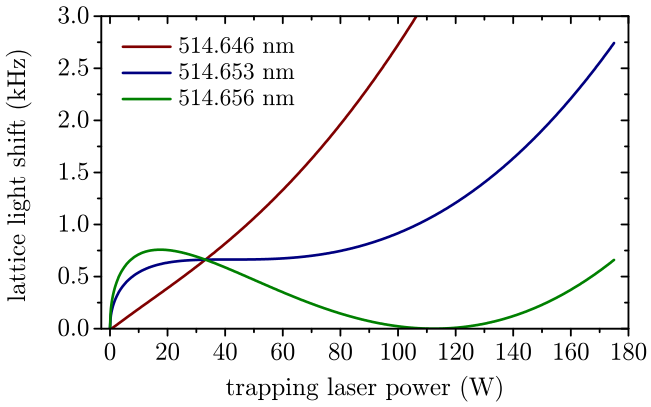

FIG. 17. Lattice light shift of the $1S$-$2S$ transition due to the optical potential following Ref. [91]. The atoms are assumed to be in a standing wave lattice's vibrational longitudinal ground state with a waist radius of $w_0 = 50\,\mu$m. Different wavelengths are presented. Red: The magic wavelength discussed in VI. Green: An operational magic wavelength where the shifts and first derivative go to zero. Blue: An operational magic wavelength where both the first and second derivatives with respect to the trapping power are canceled.

The vibrational modes of the trapped atoms and transitions between them modify the light shift. The resulting lattice light shift depends on the trapping laser parameters such as waist radius, power, and whether a running or standing wave is employed. By plugging (41) and (42) into Eq. (12) of Ref. [91], we can compute the lattice light shift of the $1S$-$2S$ clock transition.

In contrast to other lattice clocks, the lattice light shift can be computed very accurately. There are several ways to make use of this property. We can precisely pick a light shift curve by shifting the trapping laser wavelength away from the magic wavelength given in Sec. VI. Three examples are shown in Fig. 17. At an operational magic wavelength of 514.656 nm, the (green) curve possesses a maximum and a minimum with known values of the light shift. Another operational magic wavelength of 514.653 nm, shown in the (blue) curve in Fig. 17, has an inflection point where both the first and the second derivative, with respect to the intensity, cancel out. In that case, the uncertainty of the $1S$-$2S$ transition frequency depends on the trapping laser intensity only in the third order.

Experimentally, the power axis cannot be known very well, also because the laser waist radius cannot be measured with very high accuracy. However, this lack of knowledge only scales the power axis without affecting the light shift axis in these curves. The maximum, minimum, and inflection values are fixed by the trapping laser wavelength. Assuming one can determine the power axis scaling within a fractional uncertainty of 1%, we expect a total shift of 660 Hz with an uncertainty of 1.5×10^{-19} in fractional units when tuning to the inflection point of the blue curve in Fig. 17.

To determine the power axis scaling, we will measure the clock transition frequency at various laser powers. Fitting

[4]Note that this is different for the Yb and Sr lattice clocks as upper clock levels are given by a fine-structure triplet that is connected with an $E2$ matrix element with a much smaller detuning of the trapping laser.

TABLE II. Estimated corrections and uncertainties in fractional units for the proposed 1*S*-2*S* hydrogen clock. We assume that the optical power can be stabilized to within 1%, stray magnetic fields to 1%, and stray electric field to 50%. The dc Stark shift is the leading systematic and requires precise field compensation and cancellation. The large lattice light shift can be calculated to the required accuracy such that the uncertainty only comes from the uncertainty in the trapping laser power.

Effect	Correction	Uncertainty
dc Stark	9×10^{-17}	5×10^{-17}
Collisional shift	-8×10^{-17}	2×10^{-17}
BBR	-4×10^{-16}	6×10^{-18}
Zeeman	5×10^{-16}	5×10^{-18}
Probe shift	1×10^{-16}	1×10^{-18}
Pressure shift	-2×10^{-19}	2×10^{-19}
Lattice light shift	2.7×10^{-13}	1.5×10^{-19}
Second-order Doppler	1×10^{-17}	1×10^{-19}
Total		5.4×10^{-17}

these data to our theoretical model will allow us to identify the inflection point of the curve, providing a reliable reference for accurate power calibration. This method is similar to the compensation of the dc Stark shift described above, except that the compensation point is not at zero but at some precisely computable offset. Note that these methods do not require measurements of the trapping laser intensity or the determination of the trap frequencies.

VIII. CONCLUSION

In this proposal, we introduced a new method for trapping atomic hydrogen. Our method, relying on magnetic deceleration, velocity-selective deflection, and photon recoil-assisted loading, offers a promising solution for loading hydrogen atoms into an optical dipole trap without laser cooling. The estimated efficiency of our loading scheme is summarized in Table I. One of the first challenges would be establishing whether we have a high enough flux of low-velocity atomic hydrogen in our cryogenic atomic beam.

We also discussed the potential for developing a hydrogen optical atomic clock, which could significantly advance high-precision timekeeping and fundamental tests of QED. Our preliminary estimate of the clock's uncertainty put the hydrogen optical clock at a precision level of 10^{-17} as detailed in Table II. The leading systematic uncertainty is the dc Stark effect. Our proposed methods represent a novel approach to trapping atomic hydrogen and advancing atomic physics. Future work will focus on addressing the uncertainties and validating the effectiveness of these techniques through experimentation.

ACKNOWLEDGMENTS

We acknowledge stimulating discussions with Hidetoshi Katori, Paolo Crivelli, Monika Aidelsburger, and Ulrich Jentschura. This work has been supported by the Max–Planck–RIKEN–PTB–Center for Time, Constants, and Fundamental Symmetries. This work has been funded by the Deutsche Forschungsgemeinschaft (DFG, German Research Foundation), Grant No. 534953889; by the Munich Center for Quantum Science and Technology (MCQST), (EXC-2111/Project-ID: 390814868), and the ERC advanced grant Project No. 101141942 H-SPECTR. R.P. acknowledges support from the Deutsche Forschungsgemeinschaft PRISMA+Cluster of Excellence (EXC 2118/1, DFG ID 39083149). The ideas presented in the work emerged from discussions over several years with many people.

DATA AVAILABILITY

The data that support the findings of this article are not publicly available upon publication because it is not technically feasible and/or the cost of preparing, depositing, and hosting the data would be prohibitive within the terms of this research project. The data are available from the authors upon reasonable request.

APPENDIX

1. Trapping Monte Carlo

The atoms are assumed to start in the 2*S* state and are either quenched to the ground state or ionized. If quenched, then an atom is either trapped or lost. Therefore, we do not need to include superpositions requiring techniques like the Monte Carlo wave-function method. To describe the internal state of the atoms, either the optical Bloch equations or rate equations may be employed. These equations are solved numerically along with the Newtonian equation of motion. The trapping laser intensity provides the potential for Newtonian terms and simultaneously determines the internal degrees of freedom dynamics.

A few things need to be added to the simple two-level optical Bloch equations for the 2*S* and 3*P* levels to describe the full system. Two additional levels must be considered: the 1*S* state and the continuum. These can be treated as reservoirs without coherent terms with the other levels. The Newtonian motion uses the force on the 2*S* level only. This is because the trajectory ends when the atom is quenched to the 1*S* state or ionized. The force on the 3*P* level may differ from that on the 2*S* level. However, if we assume that the 3*P* level is occupied only briefly (if at all), then we may ignore that difference. The resulting optical Bloch equations are expressed using the usual density matrix:

$$\begin{aligned}
\dot{\rho}_{\mathrm{gg}} &= -\Omega\,\mathrm{Im}(\rho_{\mathrm{ge}}) - (\Gamma_{2s1s}+\Gamma_{i2s})\rho_{\mathrm{gg}} + \Gamma_{3p2s}\rho_{\mathrm{ee}} \\
\dot{\rho}_{\mathrm{ge}} &= -i\delta\rho_{\mathrm{ge}} + i\frac{\Omega}{2}(\rho_{\mathrm{gg}}-\rho_{\mathrm{ee}}) \\
&\quad -\frac{1}{2}(\Gamma_{2s1s}+\Gamma_{i2s}+\Gamma_{i3p}+\Gamma_{3p2s}+\Gamma_{3p1s})\rho_{\mathrm{ge}} \\
\dot{\rho}_{\mathrm{ee}} &= +\Omega\,\mathrm{Im}(\rho_{\mathrm{ge}}) - (\Gamma_{3p1s}+\Gamma_{3p2s}+\Gamma_{i3p})\rho_{\mathrm{ee}} \\
\dot{\rho}_{1s} &= +\Gamma_{2s1s}\rho_{1s} + \Gamma_{3p1s}\rho_{\mathrm{ee}}
\end{aligned} \tag{A1}$$

The parameters are as follows: ρ_{gg} and ρ_{ee} are the population of the 2*S* and 3*P* states, respectively. The $2\mathrm{S}(F=M=0)-3P_{3/2}(F=1,M=0)$ Rabi frequency for linear polarized light is given by $\Omega = 1.445 a_0 e E_q/\hbar$ [87] with the electric field of the quenching laser E_q and the Bohr radius a_0. We ignore the fine structure, which may be a good approximation

if the laser is blue-detuned relative to the uppermost level of the excited state. The decay constants are labeled Γ_{xy} for the decay path $x \to y$ and Γ_{ix} for the ionization of the state x. The quenching due to the quenching laser is described by the two-level part of the optical Bloch equations (first three equations) and the spontaneous decay rates of the 3P level [119]:

$$\Gamma_{3p2s} = 22.45\,1/\mathrm{s} \quad \Gamma_{3p1s} = 167.25\,1/\mathrm{s}. \tag{A2}$$

The $3P$ level can be ionized by the trapping laser with only one photon. Hence, this channel is significant even for the fast-decaying population of the $3P$. The rate is obtained by following the method described in Ref. [77]:

$$\Gamma_{i3P} = 2.68\times10^{-3}\,\frac{1/\mathrm{s}}{\mathrm{W/m^2}}\times I_t. \tag{A3}$$

The quenching laser is only useful at a reduced trapping laser intensity to limit the loss. The remaining parameters are found in the main text.

The optical Bloch equations are completed alongside the Newtonian equation of motion. The latter can be reduced to six first-order equations by introducing the atomic velocities. The equation for ρ_{ge} may be decomposed into its real and imaginary parts, depending on the solver in use. We use the fourth-order Runge-Kutta *odint* routine from Numerical Recipes [120] that requires a real-valued set of first differential equations.

In addition to the potentials (19) provided by the trapping laser, the quenching laser with an intensity I_q generates an additional potential

$$\phi_q = \alpha_q h I_q \tag{A4}$$

for the $2S$ state with polarizabilities [22]:

$$\alpha_q = (133.22,\ 96.67,\ 48.33,\ 9.666,\ 0.9663)\,\frac{\mathrm{Hz}}{\mathrm{W/m^2}}. \tag{A5}$$

The five values are given for detunings of $\delta = 2\pi\times$ (500 MHz, 1 GHz, 2 GHz, 10 GHz, 100 GHz), respectively.

Writing the intensity of the traveling-wave trapping laser as

$$I_t = \frac{w_0^2}{w^2(z)}\,I_{0t}\,e^{-2r^2/w^2(z)} \tag{A6}$$

with

$$I_{0t} = \frac{2P_t}{\pi w_0^2} \quad \text{and} \quad r^2 = x^2 + y^2 \tag{A7}$$

as well as

$$w^2(z) = w_0^2\left(1 + \left(\frac{z}{z_R}\right)^2\right) \quad \text{and} \quad z_R = \frac{\pi w_0^2}{\lambda_t} \tag{A8}$$

we get the radial and axial components of the force:

$$F_r = \alpha_t h\,\frac{4r}{w_t^2(z)}\,I_t \tag{A9}$$

and

$$F_z = 2\alpha_t h\left(\frac{1}{w^2(z)} - \frac{2r^2}{w^4(z)}\right) z\left(\frac{w_0}{z_R}\right)^2 I_t, \tag{A10}$$

respectively.

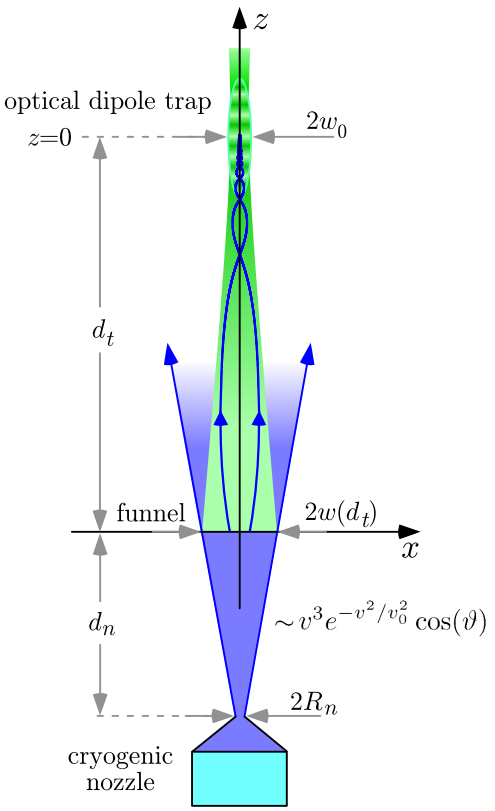

FIG. 18. Simplified geometry used in the Monte Carlo simulations.

For the knife-shaped collimated quenching laser, we assume the intensity profile:

$$I_q = I_{0q}\,e^{-2z^2/w_{0q}^2}. \tag{A11}$$

This laser crosses the trapping laser at $z = 0$ as shown in Fig. 2. To compute the $2S$-$3P$ Rabi frequency Ω, one also needs the field strength of the quenching laser:

$$E_q = \sqrt{\frac{2I_{0q}}{\varepsilon_0 c}}. \tag{A12}$$

In case the quenching laser of this form is present, the axial force acquires an additional term:

$$F_z \to F_z + \alpha_q h\,\frac{4z}{w_{0q}^2}\,I_q. \tag{A13}$$

In the case of a standing-wave trapping laser, the intensity in (A6) needs to be multiplied by

$$I_t \to I_t \times 2\cos^2(2\pi z/\lambda_t + \pi r^2/\lambda_t R(z)) \tag{A14}$$

with

$$\frac{1}{R(z)} = \frac{z}{z_R^2 + z^2}. \tag{A15}$$

While the wavefront curvature $1/R(z)$ could be important for the funneling effect in a standing wave, we ignore the Gouy phase as a tiny modification of the distances between antinodes. For numerics, working with the curvature is preferable to avoid intermediate infinities. By virtue of the factor 2 in (A14), the power is such that its spatial average is identical

to the running wave. With this choice, the averaging action of atoms moving through the standing wave can be directly compared. This does not correspond to the situation obtained with an added back-reflecting mirror.

Using a standing-wave trapping laser for the simulations, one has to remember that the result may depend on the exact launch point of the atoms, for example, at a node or antinode. The favored parameters $P_t = 1$ kW, $w_0 = 50\,\mu$m, and $d_t = 30$ cm give rise to an additional initial velocity of about 0.1 m/s.

For the simulations presented in Sec. VI C 1, we have used the simplified geometry presented in Fig. 18. In this geometry, we approximate the elliptical cross section of the deflection and trapping laser as a circle. This slightly changes the solid angle of the funneled atoms but simplifies the drawing of atoms from the distribution (8).

[1] N. Bohr, I. On the constitution of atoms and molecules, Philos. Mag. **26**, 1 (1913).

[2] W. E. Lamb and R. C. Retherford, Fine structure of the hydrogen atom by a microwave method, Phys. Rev. **72**, 241 (1947).

[3] C. G. Parthey *et al.*, Improved measurement of the hydrogen 1s–2s transition frequency, Phys. Rev. Lett. **107**, 203001 (2011).

[4] R. Pohl *et al.*, The size of the proton, Nature (London) **466**, 213 (2010).

[5] A. Antognini *et al.*, Proton structure from the measurement of 2S–2P transition frequencies of muonic hydrogen, Science **339**, 417 (2013).

[6] T. Udem, R. Holzwarth, and T. W. Hänsch, Optical frequency metrology, Nature (London) **416**, 233 (2002).

[7] A. Beyer, L. Maisenbacher, A. Matveev, R. Pohl, K. Khabarova, A. Grinin, T. Lamour, D. C. Yost, T. W. Hänsch, N. Kolachevsky, and Th. Udem, The Rydberg constant and proton size from atomic hydrogen, Science **358**, 79 (2017).

[8] A. Grinin, A. Matveev, D. C. Yost, L. Maisenbacher, V. Wirthl, R. Pohl, T. W. Hänsch, and Th. Udem, Two-photon frequency comb spectroscopy of atomic hydrogen, Science **370**, 1061 (2020).

[9] A. D. Brandt, S. F. Cooper, C. Rasor, Z. Burkley, A. Matveev, and D. C. Yost, Measurement of the $2S_{1/2}$-$8D_{5/2}$ transition in hydrogen, Phys. Rev. Lett. **128**, 023001 (2022).

[10] S. G. Karshenboim, Precision physics of simple atoms and constraints on a light boson with ultraweak coupling, Phys. Rev. Lett. **104**, 220406 (2010).

[11] C. Delaunay, C. Frugiuele, E. Fuchs, and Y. Soreq, Probing new spin-independent interactions through precision spectroscopy in atoms with few electrons, Phys. Rev. D **96**, 115002 (2017).

[12] C. Delaunay, J. P. Karr, T. Kitahara, J. C. J. Koelemeij, Y. Soreq, and J. Zupan, Self-consistent extraction of spectroscopic bounds on light new physics, Phys. Rev. Lett. **130**, 121801 (2023).

[13] R. M. Potvliege, A. Nicolson, M. P. A. Jones, and M. Spannowsky, Deuterium spectroscopy for enhanced bounds on physics beyond the standard model, Phys. Rev. A **108**, 052825 (2023).

[14] Y. Huang, H. Guan, M. Zeng, L. Tang, and K. Gao, $^{40}Ca^{+}$ ion optical clock with micromotion-induced shifts below 1×10^{-18}, Phys. Rev. A **99**, 011401(R) (2019).

[15] V. Zehnlé and J. C. Garreau, Continuous-wave Doppler cooling of hydrogen atoms with two-photon transitions, Phys. Rev. A **63**, 021402(R) (2001).

[16] D. Kielpinski, Laser cooling of atoms and molecules with ultrafast pulses, Phys. Rev. A **73**, 063407 (2006).

[17] A. M. Jayich, X. Long, and W. C. Campbell, Direct frequency comb laser cooling and trapping, Phys. Rev. X **6**, 041004 (2016).

[18] S. Wu, R. C. Brown, W. D. Phillips, and J. V. Porto, Pulsed sisyphus scheme for laser cooling of atomic (anti)hydrogen, Phys. Rev. Lett. **106**, 213001 (2011).

[19] M. Ahmadi *et al.* (The ALPHA Collaboration), Adiabatic expansion cooling of antihydrogen, Phys. Rev. Res. **6**, L032065 (2024).

[20] H. Katori, M. Takamoto, V. G. Pal'chikov, and V. D. Ovsiannikov, Ultrastable optical clock with neutral atoms in an engineered light shift trap, Phys. Rev. Lett. **91**, 173005 (2003).

[21] M. Takamoto, F. L. Hong, R. Higashi, and H. Katori, An optical lattice clock, Nature (London) **435**, 321 (2005).

[22] C. M. Adhikari, A. Kawasaki, and U. D. Jentschura, Magic wavelength for the hydrogen 1S–2S transition: Contribution of the continuum and the reduced-mass correction, Phys. Rev. A **94**, 032510 (2016).

[23] H. F. Hess, G. P. Kochanski, J. M. Doyle, N. Masuhara, D. Kleppner, and T. J. Greytak, Magnetic trapping of spin-polarized atomic hydrogen, Phys. Rev. Lett. **59**, 672 (1987).

[24] D. Kolbe, M. Scheid, and J. Walz, Triple resonant four-wave mixing boosts the yield of continuous coherent vacuum ultraviolet generation, Phys. Rev. Lett. **109**, 063901 (2012).

[25] J. M. Michan, G. Polovy, K. W. Madison, M. C. Fujiwara, and T. Momose, Narrowband solid state vuv coherent source for laser cooling of antihydrogen, Hyperfine Interact **235**, 29 (2015).

[26] G. Gabrielse *et al.*, Lyman-α source for laser cooling antihydrogen, Opt. Lett. **43**, 2905 (2018).

[27] I. D. Setija, H. G. C. Werij, O. J. Luiten, M. W. Reynolds, T. W. Hijmans, and J. T. M. Walraven, Optical cooling of atomic hydrogen in a magnetic trap, Phys. Rev. Lett. **70**, 2257 (1993).

[28] C. L. Cesar, D. G. Fried, T. C. Killian, A. D. Polcyn, J. C. Sandberg, I. A. Yu, T. J. Greytak, D. Kleppner, and J. M. Doyle, Two-photon spectroscopy of trapped atomic hydrogen, Phys. Rev. Lett. **77**, 255 (1996).

[29] D. G. Fried, T. C. Killian, L. Willmann, D. Landhuis, S. C. Moss, D. Kleppner, and T. J. Greytak, Bose-Einstein condensation of atomic hydrogen, Phys. Rev. Lett. **81**, 3811 (1998).

[30] J. Ahokas *et al.*, A large octupole magnetic trap for research with atomic hydrogen, Rev. Sci. Instrum. **93**, 023201 (2022).

[31] A. Semakin, J. Ahokas, O. Hanski *et al.*, Cold source of atomic hydrogen for loading large magnetic traps, Eur. Phys. J. D **79**, 23 (2025).

[32] S. D. Hogan, A. W. Wiederkehr, H. Schmutz, and F. Merkt, Magnetic trapping of hydrogen after multistage Zeeman deceleration, Phys. Rev. Lett. **101**, 143001 (2008).

[33] M. Ahmadi *et al.* (The ALPHA Collaboration), Observation of the hyperfine spectrum of antihydrogen, Nature (London) **548**, 66 (2017).

[34] M. Ahmadi *et al.* (The ALPHA Collaboration), Characterization of the 1S–2S transition in antihydrogen, Nature (London) **557**, 71 (2018).

[35] E. K. Anderson *et al.* (The ALPHA Collaboration), Observation of the effect of gravity on the motion of antimatter, Nature (London) **621**, 716 (2023).

[36] C. J. Baker *et al.* (The ALPHA Collaboration), Laser cooling of antihydrogen atoms, Nature (London) **592**, 35 (2021).

[37] I. C. Lane, Production of ultracold hydrogen and deuterium via Doppler-cooled Feshbach molecules, Phys. Rev. A **92**, 022511 (2015).

[38] S. F.Vázquez-Carson, Q. Sun, J. Dai, D. Mitra, and T. Zelevinsky, Direct laser cooling of calcium monohydride molecules, New J. Phys. **24**, 083006 (2022).

[39] S. A. Jones, An ion trap source of cold atomic hydrogen via photodissociation of the BaH^+ molecular ion, New J. Phys. **24**, 023016 (2022).

[40] K.-H. Yoo *et al.*, Design study of an antiproton trap for the GBAR experiment, J. Inst. **17**, T10003 (2022).

[41] P. Crivelli and N. Kolachevsky, Optical trapping of antihydrogen towards an atomic anti-clock, Hyperfine Interact **241**, 60 (2020).

[42] R. Côté, M. J. Jamieson, Z.-C. Yan, N. Geum, G.-H. Jeung, and A. Dalgarno, Enhanced cooling of hydrogen atoms by lithium atoms, Phys. Rev. Lett. **84**, 2806 (2000).

[43] R. de Carvalho, N. Brahms, B. Newman, J. M. Doyle, D. Kleppner, and T. Greytak, A new path to ultracold hydrogen, Can. J. Phys. **83**, 293 (2005).

[44] A. Singh, L. Maisenbacher, Z. Lin, J. J. Axelrod, C. D. Panda, and H. Müller, Dynamics of a buffer-gas-loaded, deep optical trap for molecules, Phys. Rev. Res. **5**, 033008 (2023).

[45] J. L. Flowers, H. A. Klein, D. J. E. Knight, and H. S. Margolis, Hydrogenic Systems for Calculable Frequency Standards: Status and Options, NPL Report CBTLM 11 (2001), https://eprintspublications.npl.co.uk/1906/.

[46] O. Amit *et al.*, Proposal for a computable optical clock, J. Phys.: Conf. Ser. **2889**, 012027 (2024).

[47] J. P. Scott, R. M. Potvliege, D. Carty, and M. P. A. Jones, Trap induced broadening in a potential hydrogen lattice clock, Metrologia **61**, 025001 (2024).

[48] J. Moreno, F. Schmid, J. Weitenberg, S. G. Karshenboim, T. W. Hänsch, Th. Udem, and A. Ozawa, Toward XUV frequency comb spectroscopy of the 1S–2S transition in He^+, Eur. Phys. J. D **77**, 67 (2023).

[49] E. Shintani (The PACSs Collaboration), Proton and neutron electromagnetic form factor and charge radius in lattice QCD, Hyperfine Interact **239**, 29 (2018).

[50] L. Gurung, T. J. Babij, S. D. Hogan, and D. B. Cassidy, Precision microwave spectroscopy of the positronium $n = 2$ fine structure, Phys. Rev. Lett. **125**, 073002 (2020).

[51] I. Cortinovis, B. Ohayon, L. de Sousa Borges, G. Janka, A. Golovizin, N. Zhadnov, and P. Crivelli, Update of muonium 1S–2S transition frequency, Eur. Phys. J. D **77**, 66 (2023).

[52] Boulder Atomic Clock Optical Network (BACON) Collaboration, Frequency ratio measurements at 18-digit accuracy using an optical clock network, Nature (London) **591**, 564 (2021).

[53] T. Bothwell, C. J. Kennedy, A. Aeppli, D. Kedar, J. M. Robinson, E. Oelker, A. Staron, and J. Ye, Resolving the gravitational redshift across a millimetre-scale atomic sample, Nature (London) **602**, 420 (2022).

[54] J. T. M. Walraven and I. F. Silvera, Helium–temperature beam source of atomic hydrogen, Rev. Sci. Instrum. **53**, 1167 (1982).

[55] F. Schmidt-Kaler, D. Leibfried, S. Seel, C. Zimmermann, W. König, M. Weitz, and T. W. Hänsch, High-resolution spectroscopy of the 1S–2S transition of atomic hydrogen and deuterium, Phys. Rev. A **51**, 2789 (1995).

[56] L. Maisenbacher, Precision spectroscopy of the 2SnP transitions in atomic hydrogen, Ph.D. thesis, Munich, 2020.

[57] S. F. Cooper, A. D. Brandt, C. Rasor, Z. Burkley, and D. C. Yost, Cryogenic atomic hydrogen beam apparatus with velocity characterization, Rev. Sci. Instrum. **91**, 013201 (2020).

[58] J. R. Zacharias, MIT RLE Quart. Prog. Rep. **48**, VII (1958).

[59] P. Forman, Atomichron®: The atomic clock from concept to commercial product, Proc. IEEE **73**, 1181 (1985).

[60] W. Zernik, Two-photon ionization of atomic hydrogen, Phys. Rev. **135**, A51 (1964).

[61] L. P. Rapoport, B. A. Zon, and L. P. Manakov, Two-photon ionization of the hydrogen atom, Zh. Eksp. Teor. Fiz. **56**, 400 (1969) [Sov. Phys. JETP **29**, 220 (1969)].

[62] V. Wirthl, L. Maisenbacher, J. Weitenberg, A. Hertlein, A. Grinin, A. Matveev, R. Pohl, T. W. Hänsch, and Th. Udem, Improved active fiber-based retroreflector with intensity stabilization and a polarization monitor for the near UV, Opt. Express **29**, 7024 (2021).

[63] V. Wirthl, L. Maisenbacher, J. Weitenberg, A. Hertlein, A. Grinin, A. Matveev, R. Pohl, T. W. Hänsch, and Th. Udem, Improved active fiber-based retroreflector with intensity stabilization and a polarization monitor for the near UV: Erratum, Opt. Express **30**, 7340 (2022).

[64] H. Fleurbaey, S. Galtier, S. Thomas, M. Bonnaud, L. Julien, F. Biraben, F. Nez, M. Abgrall, and J. Guéna, New measurement of the 1S–3S transition frequency of hydrogen: Contribution to the proton charge radius puzzle, Phys. Rev. Lett. **120**, 183001 (2018).

[65] B. McCarroll, An improved microwave discharge cavity for 2450 MHz, Rev. Sci. Instrum. **41**, 279 (1970).

[66] D. Singy, P. A. Schmelzbach, W. Grüebler, and W. Z. Zhang, Study of the surface recombination in the production of a dense polarized hydrogen atomic beam at low temperature, Nucl. Instrum. Meth. Phys. Res. Sect. B **47**, 167 (1990).

[67] N. Koch and E. Steffens, High intensity source for cold atomic hydrogen and deuterium beams, Rev. Sci. Instrum. **70**, 1631 (1999).

[68] H. Pauly, *Atomic and Molecular Beam Methods* (Oxford University Press, Oxford, 1988), Vol. 1.

[69] N. F. Ramsey, *Molecular Beams* (Oxford University Press, Oxford, 1956).

[70] R. A. Naumann and H. H. Stroke, Apparatus Upended: A short history of the fountain A–Clock, Phys. Today **49**(5), 89 (1996).

[71] I. Estermann, O. C. Simpson, and O. Stern, The Free Fall of atoms and the measurement of the velocity distribution in a molecular beam of cesium atoms, Phys. Rev. **71**, 238 (1947).

[72] T. G. Tiecke, S. D. Gensemer, A. Ludewig, and J. T. M. Walraven, High-flux two-dimensional magneto-optical-trap source for cold lithium atoms, Phys. Rev. A **80**, 013409 (2009).

[73] A. Matveev, N. Kolachevsky, C. M. Adhikari, U. D. Jentschura, Pressure shifts in high-precision hydrogen spectroscopy: II. Impact approximation and Monte-Carlo simulations, J. Phys. B: At. Mol. Opt. Phys. **52**, 075006 (2019).

[74] N. R. Kestner and H. Margenau, *Theory of Intermolecular Forces* (Pergamon Press, Oxford, 1969).

[75] J. Vanier and C. Audoin, *The Quantum Physics of Atomic Frequency Standards* (CRC Press, Boca Raton, FL, 1989).

[76] L. M. García, J. Chaboy, F. Bartolomé, and J. B. Goedkoop, Orbital magnetic moment instability at the spin reorientation transition of $Nd_2Fe_{14}B$, Phys. Rev. Lett. **85**, 429 (2000).

[77] M. Haas *et al.*, Two-photon excitation dynamics in bound two-body Coulomb systems including ac Stark shift and ionization, Phys. Rev. A **73**, 052501 (2006).

[78] S. F. Cooper, Z. Burkley, A. D. Brandt, C. Rasor, and D. C. Yost, Cavity-enhanced deep ultraviolet laser for two-photon cooling of atomic hydrogen, Opt. Lett. **43**, 1375 (2018).

[79] Z. Burkley, L. de Sousa Borges, B. Ohayon, A. Golovizin, J. Zhang, and P. Crivelli, Stable high power deep-uv enhancement cavity in ultra-high vacuum with fluoride coatings, Opt. Express **29**, 27450 (2021).

[80] J. C. Garreau, M. Allegrini, L. Julien, and F. Biraben, High resolution spectroscopy of the hydrogen atom. II. Study of line profiles, J. Phys. France **51**, 2275 (1990).

[81] W. Gerlach and O. Stern, Der experimentelle Nachweis des magnetischen Moments des Silberatoms, Z. Phys. **8**, 110 (1922).

[82] J. R. Gardner, E. M. Anciaux, and M. G. Raizen, Communication: Neutral atom imaging using a pulsed electromagnetic lens, J. Chem. Phys. **146**, 081102 (2017).

[83] G. Grynberg, F. Biraben, and B. Cagnac, Doppler-free two-photon spectroscopy of neon. II. Line intensities, J. Phys. France **38**, 629 (1977).

[84] W. G. Kaenders, F. Lison, I. Müller, A. Richter, R. Wynands, and D. Meschede, Refractive components for magnetic atom optics, Phys. Rev. A **54**, 5067 (1996).

[85] S. Federmann, A spin-flip cavity for microwave spectroscopy of antihydrogen, Ph.D. thesis, Wien University, 2012.

[86] V. Polyakov, Y. Timofeev, and N. Demidov, Frequency stability improvement of an active hydrogen maser with a single-state selection system, in *Proceedings of the 2021 Joint Conference of the European Frequency and Time Forum and IEEE International Frequency Control Symposium (EFTF/IFCS), Gainesville, FL, USA* (IEEE, Piscataway, NJ, 2021), pp. 1–4.

[87] H. A. Bethe and E. E. Salpeter, *Quantum Mechanics of One– and Two–Electron Atoms* (Springer, Berlin, 1957).

[88] D. Budker, D. F. Kimball, and D. P. DeMille, *Atomic Physics: An Exploration Through Problems and Solutions* (Oxford University Press, Oxford, 2008).

[89] U. D. Jentschura, C. M. Adhikari, R. Dawes, A. Matveev, and N. Kolachevsky, Pressure shifts in high-precision hydrogen spectroscopy. I. Long-range atom–atom and atom–molecule interactions, J. Phys. B: At. Mol. Opt. Phys. **52**, 075005 (2019).

[90] A. Aeppli, K. Kim, W. Warfield, M. S. Safronova, and J. Ye, Clock with 8×10^{-19} systematic uncertainty, Phys. Rev. Lett. **133**, 023401 (2024).

[91] H. Katori, V. D. Ovsiannikov, S. I. Marmo, and V. G. Palchikov, Strategies for reducing the light shift in atomic clocks, Phys. Rev. A **91**, 052503 (2015).

[92] J. Dalibard and C. Cohen–Tannoudji, Laser cooling below the Doppler limit by polarization gradients: Simple theoretical models, J. Opt. Soc. Am. B **6**, 2023 (1989).

[93] M. Falkenau, V. V. Volchkov, J. Rührig, A. Griesmaier, and T. Pfau, Continuous loading of a conservative potential trap from an atomic beam, Phys. Rev. Lett. **106**, 163002 (2011).

[94] S. Karshenboim *et al.* (unpublished).

[95] J. Sommerfeldt, R. A. Müller, A. V. Volotka, S. Fritzsche, and A. Surzhykov, Vacuum polarization and finite-nuclear-size effects in the two-photon decay of hydrogenlike ions, Phys. Rev. A **102**, 042811 (2020).

[96] C. Cohen–Tannoudji, in *Proceedings Les Houches Summer School Session LIII 1990*, edited by J. Dalibard and J. M. Raimond (Elsevier Science Publishers B.V., 1992).

[97] M. A. Norcia, A. W. Young, W. J. Eckner, E. Oelker, J. Ye, and A. M. Kaufman, Seconds-scale coherence on an optical clock transition in a tweezer array, Science **366**, 93 (2019).

[98] I. S. Madjarov, A. Cooper, A. L. Shaw, J. P. Covey, V. Schkolnik, T. H. Yoon, J. R. Williams, and M. Endres, An atomic-array optical clock with single-atom readout, Phys. Rev. X **9**, 041052 (2019).

[99] J. E. Bjorkholm, Collision-limited lifetimes of atom traps, Phys. Rev. A **38**, 1599 (1988).

[100] M. Ben Dahan, E. Peik, J. Reichel, Y. Castin, and C. Salomon, Bloch oscillations of atoms in an optical potential, Phys. Rev. Lett. **76**, 4508 (1996).

[101] I. F. Silvera and J. T. M. Walraven, Stabilization of atomic hydrogen at low temperature, Phys. Rev. Lett. **44**, 164 (1980).

[102] H. J. Manetsch, G. Nomura, E. Bataille, K. H. Leung, X. Lv, and M. Endres, A tweezer array with 6100 highly coherent atomic qubits, arXiv:2403.12021.

[103] O. J. Luiten, M. W. Reynolds, and J. T. M. Walraven, Kinetic theory of the evaporative cooling of a trapped gas, Phys. Rev. A **53**, 381 (1996).

[104] A. J. Olson, R. J. Niffenegger, and Y. P. Chen, Optimizing the efficiency of evaporative cooling in optical dipole traps, Phys. Rev. A **87**, 053613 (2013).

[105] M. J. Jamieson, A. Dalgarno, and J. N. Yukich, Elastic scattering of hydrogen atoms at low temperatures, Phys. Rev. A **46**, 6956 (1992).

[106] C. L. Cesar and D. Kleppner, Two-photon Doppler-free spectroscopy of trapped atoms, Phys. Rev. A **59**, 4564 (1999).

[107] G. J. Dick, Local oscillator induced instabilities in trapped ion frequency standards, in *Proceedings of the 34th Annual Precise Time and Time Interval Systems and Applications Meeting* (ION, Redondo Beach, CA, 1987), pp. 133–147.

[108] R. Grimm, M. Weidemüller, and Y. B. Ovchinnikov, Optical dipole traps for neutral atoms, Adv. At. Mol. and Opt. Phys. **42**, 95 (2000).

[109] U. D. Jentschura and M. Haas, Reexamining blackbody shifts for hydrogenlike ions, Phys. Rev. A **78**, 042504 (2008).

[110] G. Hagel, R. Battesti, F. Nez, L. Julien, and F. Biraben, Observation of a motional Stark effect to determine the second-order Doppler effect, Phys. Rev. Lett. **89**, 203001 (2002).

[111] D. H. McIntyre, R. G. Beausoleil, C. J. Foot, E. A. Hildum, B. Couillaud, and T. W. Hänsch, Continuous-wave measurement of the hydrogen 1S–2S transition frequency, Phys. Rev. A **39**, 4591 (1989).

[112] T. C. Killian, D. G. Fried, L. Willmann, D. Landhuis, S. C. Moss, T. J. Greytak, and D. Kleppner, Cold collision frequency shift of the 1s–2s transition in hydrogen, Phys. Rev. Lett. **81**, 3807 (1998).

[113] J. W. Farley and W. H. Wing, Accurate calculation of dynamic Stark shifts and depopulation rates of Rydberg energy levels induced by blackbody radiation. Hydrogen, helium, and alkali-metal atoms, Phys. Rev. A **23**, 2397 (1981).

[114] I. Ushijima, M. Takamoto, M. Das, T. Ohkubo, and H. Katori, Cryogenic optical lattice clocks, Nat. Photon. **9**, 185 (2015).

[115] A. V. Taichenachev, V. I. Yudin, V. D. Ovsiannikov, V. G. Pal'chikov, and C. W. Oates, Frequency shifts in an optical lattice clock due to magnetic-dipole and electric-quadrupole transitions, Phys. Rev. Lett. **101**, 193601 (2008).

[116] I. Ushijima, M. Takamoto, and H. Katori, Operational magic intensity for sr optical lattice clocks, Phys. Rev. Lett. **121**, 263202 (2018).

[117] R. C. Brown *et al.*, Hyperpolarizability and operational magic wavelength in an optical lattice clock, Phys. Rev. Lett. **119**, 253001 (2017).

[118] A. Derevianko and H. Katori, *Colloquium*: Physics of optical lattice clocks, Rev. Mod. Phys. **83**, 331 (2011).

[119] NIST Atomic Spectra Database: https://www.nist.gov/pml/atomic-spectra-database.

[120] B. P. Flannery, W. H. Press, S. A. Teukolsky, and V. T. Vetterling, *Numerical Recipes in Pascal (First Edition): The Art of Scientific Computing* (Cambridge University Press, Cambridge, UK, 1991).